Appendix E
FCT Document Cover Sheet

Name/Title of Deliverable/Milestone: Fluid Flow Modeling In Representative Media
Work Package Title and Number: Generic Natural Systems Evaluation - LANL
Work Package WBS Number: FT-13LA080704
Responsible Work Package Manager: Scott Painter Scott Painter
(Name/Signature)

Date Submitted 12/15/2012

Quality Rigor Level for Deliverable/Milestone	☒ QRL-3	☐ QRL-2	☐ QRL-1 ☐ Nuclear Data	☐ N/A*

This deliverable was prepared in accordance with Los Alamos National Laboratory
(Participant/National Laboratory Name)

QA program which meets the requirements of
☒ DOE Order 414.1 ☐ NQA-1-2000

This Deliverable was subjected to:

☒ Technical Review	☐ Peer Review
Technical Review (TR)	**Peer Review (PR)**
Review Documentation Provided	**Review Documentation Provided**
☐ Signed TR Report or,	☐ Signed PR Report or,
☐ Signed TR Concurrence Sheet or,	☐ Signed PR Concurrence Sheet or,
☒ Signature of TR Reviewer(s) below	☐ Signature of PR Reviewer(s) below

Name and Signature of Reviewers
Zhenxue Dai

*Note: In some cases there may be a milestone where an item is being fabricated, maintenance is being performed on a facility, or a document is being issued through a formal document control process where it specifically calls out a formal review of the document. In these cases, documentation (e.g., inspection report, maintenance request, work planning package documentation or the documented review of the issued document through the document control process) of the completion of the activity along with the Document Cover Sheet is sufficient to demonstrate achieving the milestone. QRL for such milestones may be also be marked N/A in the work package provided the work package clearly specifies the requirement to use the Document Cover Sheet and provide supporting documentation.

Fluid Flow Model Development for Representative Geologic Media

Fuel Cycle Research & Development

Prepared for
U.S. Department of Energy
Used Fuel Disposition Campaign

Scott Painter
Carl Gable
Nataliia Makedonska
Jeffrey Hyman
Tsung-Lin Hsieh
Quan Bui
Los Alamos National Laboratory

H.H. Liu
Jens Birkholzer
Lawrence Berkeley National Laboratory

December 2012

LA-UR-12-26878 FCRD-UFD-2013-000058

SUMMARY

Clay and granitic media are potential host media for future repositories for used nuclear fuel. This report addresses the representation of flow in these two media within numerical process models.

For granitic rock, flow is primarily in relatively sparse networks of fractures. Discrete fracture network (DFNs) models are an approach to representing flow in fractured granite that explicitly represents the geometry and flow properties of individual fractures. The DFN approach captures important flow phenomena that are difficult to represent in conventional equivalent continuum approaches. However, the DFN approach is computationally demanding and requires care in constructing computational meshes. New DFN generation and computational grid generation methods have been developed and tested. The approach places constraints on the generation of the DFN. These constraints make it possible to create high-quality computational meshes that enable accurate flow and transport solutions on the generated DFNs. Mesh generation is one component of the DFN-based computational workflow. Preliminary work on a second component of the workflow – the generation of flow streamlines within the DFN – is also summarized. Future work will focus on the completion of the particle tracking capability and development of parallel high-performance computing capability to model flow on the large grids needed to describe the DFN. Application studies using data from select field sites is also needed to understand how the new tools can be used in practice.

Water flow in clay media is another important process. Experimental results indicate that the traditional form of Darcy’s law is not adequate for describing water flow processes in clay media because the observed relationship between water flux and hydraulic gradient can be highly non-linear. To capture this non-Darcian flow behavior, a new relationship between water flux and hydraulic gradient was created by generalizing the currently existing relationships. The new relationship is shown to be consistent with experimental observations for both saturated and unsaturated conditions. An empirical relationship between permeability and the threshold hydraulic gradient, an important measure of non-Darcian behavior, was also developed. The latter relationship is practically useful because it can reduce the number of parameters whose values need to be determined from experiment data in order to model non-Darcian behavior. Future work will address the incorporation of temperature and electrolyte concentrations into the proposed relationships.

CONTENTS

FIGURES

Acronyms

UFDC	Used Fuel Disposition Campaign
R&D	Research and Development
DFN	Discrete Fracture Network
PSLG	Planar Straight Line Graph
MD	Molecular Dynamics

FLUID FLOW MODEL DEVELOPMENT IN REPRESENTATIVE GEOLOGIC MEDIA

1. INTRODUCTION

The U.S. Department of Energy Office of Nuclear Energy, Office of Fuel Cycle Technology has established the Used Fuel Disposition Campaign (UFDC) to conduct research and development (R&D) activities related to storage, transportation and disposal of used nuclear fuel and high-level nuclear waste.

The UFDC is currently evaluating generic research issues affecting the viability of repositories in three geologic media (salt, clay, and crystalline rock). Consistent with the well-accepted multiple barrier concept for waste repository safety, repository systems include both natural and engineered barriers. From this perspective, the natural barrier needs to be evaluated and necessary research conducted to ensure adequate safety function. Consistent with the broader objectives of the UFDC, R&D is being conducted to develop (1) fundamental understanding of natural system performance in a range of environments, and (2) computational modeling capability for evaluating natural system performance.

The R&D Roadmap for UFDC Natural System Evaluation and Tool Development (Wang, 2011) identified fluid flow in fractured crystalline rock and in low-permeability clay material as priority R&D topics for the UFDC Natural System Evaluation and Tool Development work package. This report summarizes flow model development for those two representative geologic media. Section 2 provides a summary of UFDC work to develop advanced flow modeling approaches for fractured crystalline rock based on explicitly represented fractures (Contributors: S. Painter, C. Gable, N. Makedonska, J. Hyman, Q. Bui, T.-L. Hseih from Los Alamos National Laboratory). Section 3 summarizes modeling approaches for non-Newtonian flow in clays (Contributors: H.-H. Liu and Jens Birkholzer from Lawrence Berkeley National Laboratory).

2. DEVELOPMENT OF FLOW AND TRANSPORT MODELS FOR DISCRETELY FRACTURED MEDIA

2.1 Introduction

Relatively impermeable hard rocks such as fractured granite and fractured welded tuffs have been considered previously as potential repository host media. Fractures are ubiquitous in such media and provide the primary migration pathways for radionuclides. Experience has shown that flow and transport in fractured rock is rarely described adequately by uniform or mildy nonuniform isotropic continuum representations (Neuman 2005) and a range of alternatives to the classical continuum representation have been developed. These alternative approaches may be grouped into three general classes: discrete fracture network representations, complex continua representations, and hybrid representations.

Discrete fracture network (DFN) models depict the rock mass as an interconnected network of explicitly represented fractures. The approach is in the reductionist tradition, implicitly assuming that detailed statistical descriptions of small observable features will, once combined in numerical simulations, lead to understanding of the system as a whole. Networks of fractures are first stochastically generated using a stochastic model derived from site data. A computational mesh is placed on each fracture plane usually ensuring that the mesh on each of a pair of intersecting fractures matches along the intersection. Groundwater flow equations are then solved using this computational mesh. The final step is then to simulate radionuclide transport using the computed flow field, usually by particle tracking. Most large-scale applications do not explicitly mesh the matrix volumes between adjacent fractures. Instead the effects of diffusion into the unrepresented matrix volume are represented (modeled) in the transport step (see e.g. Painter et al. 2008). DFN simulations were introduced first in theoretical studies; feasibility of detailed site-specific applications has also been clearly demonstrated (e.g. Cvetkovic et al. 2004, Svensk Kärnbränslehantering 2011).

Complex continua representations generalize a simple effective continuum representation to account for various flow and transport phenomena. Dual continuum models (Barenblatt et al. 1960; Warren and Root 1963) represent fractured porous rock as two overlapping and interacting continua. In its most general form (e.g. Duguid and Lee, 1977), known as the dual permeability model, flow and transport takes place in both the fracture and matrix continua while accounting for fluid and solute migration between the two continua in response to pressure and concentration differences. Commonly, flow in the matrix system is neglected relative to flow in the fracture system. In this case, the matrix acts as a non-conductive reservoir for fluid and/or solute storage and the fracture system provides the fluid migration pathways. In this variant, usually referred to as the dual porosity model, fluid and solute flux are proportional to the pressure and concentration differences between the two continua at a given location and time. The dual continuum class of models has also been generalized (Pruess and Narasimhan 1985; Zyvoloski et al. 2008) to better represent gradients internal to the matrix blocks. In this approach, multiple continua are used to represent matrix processes. Flow between spatially adjacent matrix cells may be included or not represented, depending on the variant.

Regardless of how the matrix/fracture interactions are represented, multiple continuum models originally conceptualized the fracture flow system as having a representative elementary volume (REV) that establishes a spatial scale above which the flow properties become approximately independent of scale.

For natural fracture patterns, which often have a broad distribution of fracture lengths, the existence of a classical REV scale may be questionable. Neuman proposed a stochastic continuum approach that does not require an REV (Neuman 1987, 2005). In his approach, an effective permeability tensor and other required flow/transport properties are assigned to each grid block in a conventional continuum conceptualization. However, the properties vary from grid cell to grid cell according to a stochastic model. Moreover, the stochastic model is dependent on the size of the grid block. Thus, a different stochastic model is required if the spatial discretization is changed. Parameterization of a stochastic continuum model, which generally requires inverse modeling of multiple pressure interference and solute tracer tests, has been demonstrated at the Apache Leap field site (e.g. Neuman 2005). The stochastic continuum model may be combined with any of the dual or multiple continua ideas to represent fracture/matrix interactions.

Hybrid methods adopt a reductionist view similar to DFN models but also use continuum representations for practical computational reasons (e.g. to reduce the overall size of the computational mesh). Hybrid methods fall into two subclasses: nested and upscaled. In nested models, explicit DFN models are used along transport pathways or in other regions where high spatial resolution is required and continuum representations are used in regions that are of less interest. This approach allows for a DFN representation of transport in and near expected transport pathways while still modeling a sufficiently large region to honor natural hydraulic boundary conditions. In upscaled models, explicit DFN representations are constructed and stochastically generated. However, the flow problem is not solved on the full DFN. Instead, the DFN is used to establish, grid block by grid block, equivalent permeability tensors for use in a continuum model. Jackson et al. (2000), Svensson (2001) and Botros et al. (2008) provide examples of upscaling algorithms for the permeability tensors. Experience with upscaled models for flow has generally been good, but the approach is questionable for transport. Extensions that attempt to recover the transport effects of subgrid velocity variability through stochastic simulation have emerged (Painter and Cvetkovic 2005) but have not been fully explored.

Experience suggests that it should be possible to model a sufficiently well-characterized site in a variety of ways and that combinations of methods may allow for the most efficient use of available information. Extensive studies by the Swedish Nuclear Fuel and Waste Management Company in support a safety case for a proposed spent fuel repository (Svensk Kärnbränslehantering 2011) has clearly demonstrated practical utility of hybrid approaches to flow and transport modeling. Given this experience it is likely that DFN and DFN/continuum hybrids will play an important role in future assessments of fractured hard rock sites. However, modern and non-proprietary modeling tools for supporting such assessments and for addressing key unresolved scientific issues are lacking.

This Chapter addresses Topic P1 of the R&D Plan for UFDC Natural Systems Evaluation and Tool Development – Development of Discrete Fracture Models. The longer-term objective is to develop discrete fracture network (DFN) flow and transport modeling capability, which was identified as a capability gap. The initial stages of the DFN software development process related to requirements definition, algorithm design and prototyping were summarized in FY2011 report. This chapter summarizes the current state of the DFN flow and transport modeling capability.

2.2 State of the Art

In order to represent a fractured media for computation of fluid flow and mass transport there are four main steps. First the fractures must be described and characterized quantitatively. This might be explicit descriptions of the shape and orientation of each fracture or it might be statistical and be expressed in terms of distributions. Second, if explicit representations of fractures are required for calculations a computational mesh representation of the fractures must be created that is both representative of the fracture system and compatible with the flow and mass transport numerical model. Third is the calculation of fluid flow that might be done on the explicit fracture network mesh or on some upscaled equivalent continuum representation. The fourth step is the calculation of radionuclide mass transport using the calculated flow field. In the remainder of this section we focus on the second step, the creation of explicit meshed representation of fracture networks, and the fourth step, representation of radionuclide transport.

The last ten years has seen an increase in the number of papers that describe specific implementations of methods to mesh 3D fracture networks. The problem if representing and mesh fracture networks in 2D is not trivial, however both in terms of computational cost and computational infrastructure, this is a solved problem. Mesh representation in three dimensions still presents difficulties. In the work of Karimi-Fard et al. (2006) constrained Delaunay meshing is employed in 2D using the software Triangle (Shewchuk 1996) and in 3D TetGen (Si 2004). In this application a 3D fracture network is constructed with planar fractures but flow is computed on an upscaled continuum. Erhel et al. (2009) develop a method to mesh large stochastically generated fracture networks by prudent modification of the fractures so that undesirable and pathological geometric configurations do not occur. Similarly, a series of recent papers (Mustapha and Dimitrakopoulos 2009, Mustapha 2010, Mustapha et al. 2010) outlines methods to mesh fracture networks in 3D with intersecting triangulations. These papers take the approach of modifying the fracture network geometry to create fracture representations that are more easily turned into discrete mesh representations. However, the result is non-planar triangulations, which introduces some difficulties when applying the mesh to some flow and mass transport discretizations.

There are a number of software packages available for characterization, meshing and computations. Some of these are listed and briefly described below.

FracMan, www.fracturedreservoirs.com. Fracture network characterization and generation from observations or statistical representations; meshing of fracture networks and upscaling DFN flow properties to equivalent porous medium parameters. The associated MAFIC module has some flow and transport capabilities, but according to the company website, it is generally applicable only to relatively small networks.

DFNModeler, Geological Survey of Alabama. http://www.gsa.state.al.us/CO2/DFNModeler/dfnm.htm. Fracture network characterization and representation of interpretation of compartmentalization of coal bed methane formations.

MShale www.mfrac.com. Orthogonal fracture network generation. Designed for computing stress strain for coal bed methane formations.

Petrel, Schumberger, http://www.slb.com/services/software/geo/petrel.aspx. Fracture characterization and representation. Upscaled representation of matrix can be represented in Eclipse reservoir simulation package.

Rockflow, http://www.rockflow.de. Simulation of Flow, Mass and Heat Transfer and Deformation in Fractured Porous Rock.

CONNECTFLOW (Joyce et al 2011)**,** Serco Assurance, connectflow.com. Three-dimensional DFN generation and flow/transport modeling; hybrid DFN/continuum modeling with nested and upscaled models. Flow and transport in large networks has been demonstrated. Transport is treated approximately.

HydroGeoSphere/FRAC3DVS www.hydrogeosphere.org. Flow and transport including discretized matrix for three-dimensional networks fractures. Limited to orthogonal fractures.

At present there does not appear to be a non-proprietary DFN flow and transport modeling tool with sufficient capabilities to support the research needs of the Used Fuel Disposition Campaign. In addition, at present, there does not appear to be a general-purpose mesh generation tool that will generate triangulations of intersecting planar fracture networks such that the resulting triangulations are conforming Delaunay triangulations. Conforming Delaunay triangulations are necessary for accurate flow/transport solutions in commonly used control volume flow codes.

2.3 Technical Approach

Three algorithmic considerations related to DFN flow and transport simulations are identified: meshing, solving for flow, and modeling radionuclide transport.

Meshing considerations. Mesh generation for DFN flow and transport simulations involves constructing a quality mesh on each fracture surface that also meets two constraints: (1) the mesh on each fracture must conform to intersections with other fractures, and (2) the meshes for each of two intersecting fraction must coincide along the intersection. The second constraint may be relaxed if mortar methods (e.g. Ewing et al. 2000, Arbogast et al. 2000, Pichot et al. 2010) are used to solve for flow and transport. Mortar methods are not addressed here.

Figure 2-1a shows a simple example of two intersecting fractures. Nodes are shown as blue dots; the triangulation of the nodes is shown with blue lines. If a finite element method is used to solve for flow, the triangles are the basic computational unit (element); each is contained within a single fracture. If a control volume method is used for the flow, the basic computational unit is the control volume. If a node is not on a fracture intersection, the associated control volume is a polygon. For nodes that lie on fracture intersections, the associated control volume lies in the planes of both fractures. The control volume for the central node in Figure 2-1a is shown in Figure 2-1b.

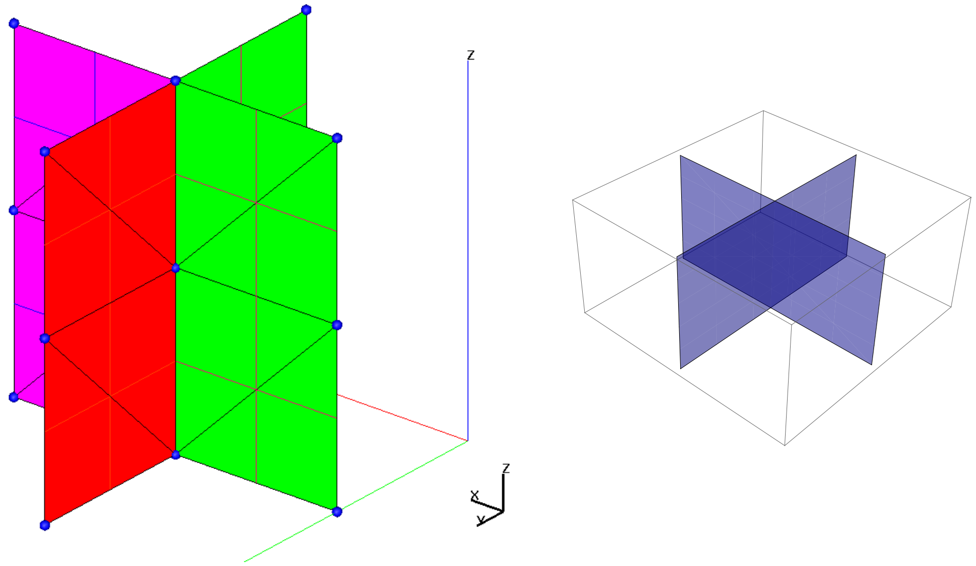

Figure 2-1. Simple example of two orthogonal intersecting planar fracture surfaces. The fracture surfaces are represented by triangles (left image). The control volume for the central node is shown on the right.

Regardless of whether the mesh is generated for use in a control volume of finite element calculation, the major meshing issues are associated with pathological cases that lead to small and or high aspect ratio cells/elements. Some examples are shown in Figure 2-2. Note that these are associated with "triple intersections" wherein a fracture intersection is intersected by a third fracture and with near misses to triple intersections.

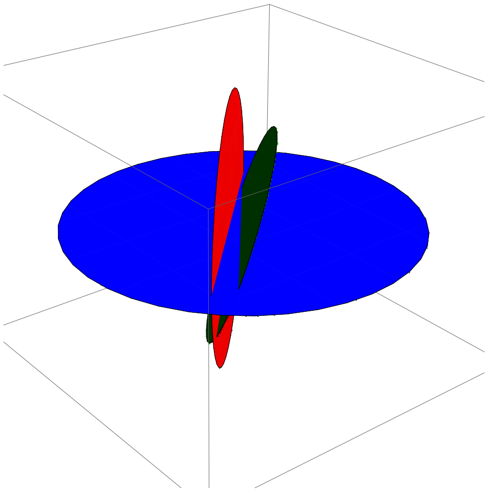

Figure 2-2. Example configuration that causes problems in meshing DFN models for flow and transport calculations. To resolve the space on the blue fracture between the black and red fractures would require very small computational elements, which causes problems with flow and transport codes. Rather than develop robust algorithms to mesh such configurations, an approach is under development that constrains the DFN based on geologic considerations to avoid these problematic configurations.

Solving for flow. Numerical methods for solving for flow within the DFN must be able to accommodate the fully unstructured grid, which is locally two-dimensional within each fracture. Three methods are identified: conventional finite elements, mixed hybrid finite elements, and control volumes.

Early 3-D DFN research codes and most existing commercial codes use the finite element method to solve for flow within the fracture network. The finite element method is able to accommodate fully unstructured grids without difficulty, but is not locally mass conserving. Lack of local mass conservation is an issue for radionuclide transport simulations because it can lead to nonphysical mass accumulation. If a particle tracking method is used for the radionuclide transport simulation, for example, lack of local mass conservation can cause particles representing packets of radionuclide mass to become stuck in the computational mesh. If enough particles become stuck a misleading representation of geosphere performance would result. Local postprocessing of the finite-element flow solution using the approach of Cordes and Kinzelbach (1992) or similar method can improve the local mass conservation dramatically. This method is difficult to implement especially at fracture intersections.

Applied to groundwater flow, the mixed hybrid finite element method (Mose et al. 1994) approximates simultaneously the hydraulic head and groundwater velocity. The number of unknowns is doubled, but the approximation to the groundwater velocity is obtained as a continuous field, thus avoiding velocity discontinuities that plague transport calculations.

The finite element method and the mixed hybrid finite element method are convenient for saturated flow but are not ideal for unsaturated or multiphase flow. Control volume methods are traditionally used for these situations. Applied to flow, the control volume method solves conservation equations for water mass on each computational cell. Applied to radionuclide transport, the control volume method solves conservation equations for radionuclide mass on each computational cell, thus avoiding any issues with local mass conservation. The computer codes FEHM (Zyvoloski 2007) and TOUGH2 (Pruess et al. 1999) are based on the control volume method.

Modeling radionuclide transport. Although the finite element, mixed hybrid finite element, or control volume method can be used to solve the advection dispersion equation to represent radionuclide transport, particle tracking on the computed groundwater velocity field is the more common approach to representing radionuclide transport in DFN modeling. Particle tracking does not produce numerical dispersion and can accommodate complex dispersivity tensors. In addition, computational strategies that include the effects of matrix diffusion and sorption by postprocessing the results of particle tracking simulations without matrix diffusion are among the most efficient and practical methods available for representing the transport effects of matrix diffusion.

2.4 Automated Delaunay Triangulation of Stochastically Generated Three Dimensional Discrete Fracture Networks

DFN models often treat fractures as quasi- two-dimensional finite features embedded in three-dimensional space. Each fracture is given a shape, orientation, and location in R^3. Fractures are the result of various geological events and are often divided into sets associated with specific geologic events, with a relatively narrow orientation distribution within each set (National Research Council, 1996). Fractures are commonly represented as ellipses or rectangles and the length of fractures is often assumed to follow a truncated power-law or a log-normal distribution. The location in three-dimensional space is taken to be stochastic due to the difficulty of directly measuring locations of fractures in the subsurface. Figure 2-3 shows a stochastically generated network of one hundred ellipses and exhibits the complexity of the intersections between fractures. For a wide variety of lengths, orientations between fracture sets (whose means may or may not be orthogonal), and stochastic location in space, the problem of generating a high-quality computational mesh is apparent.

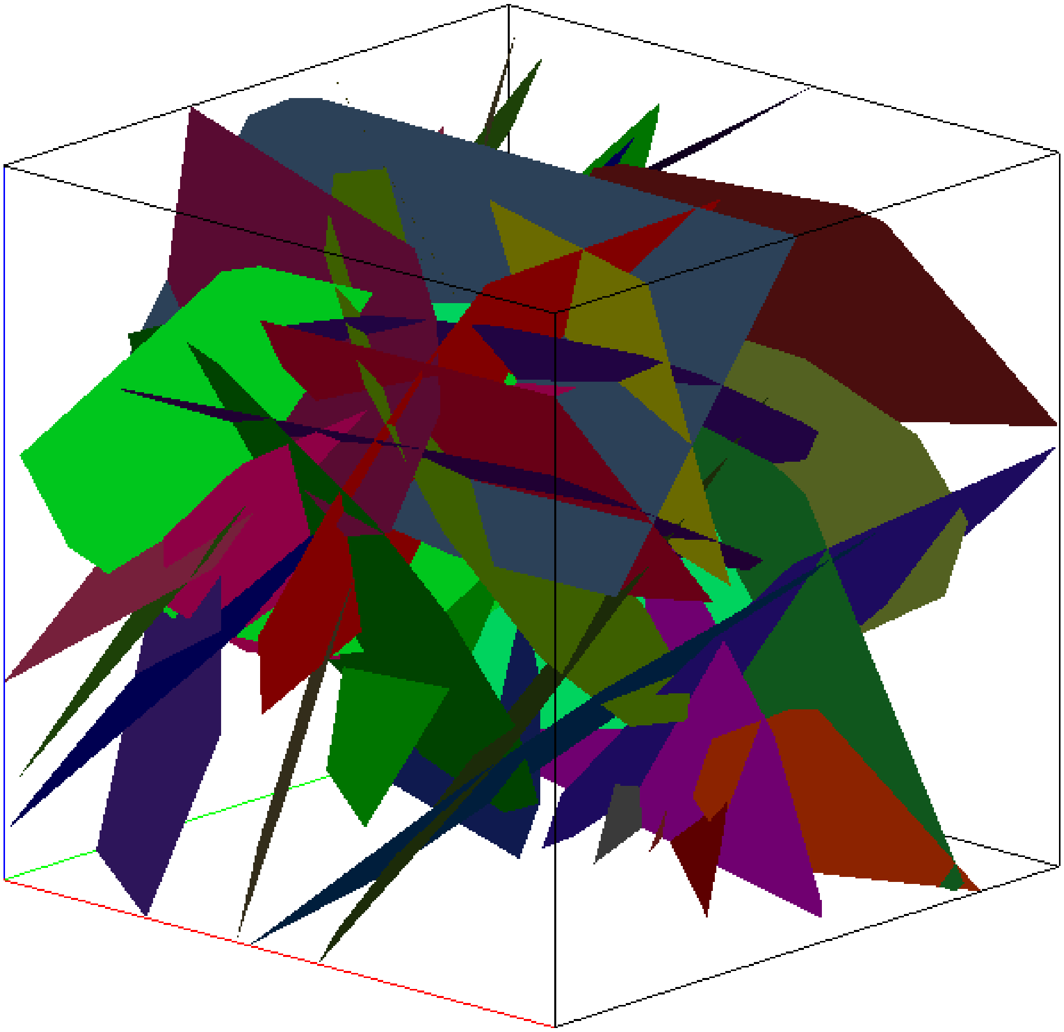

Figure 2-3. Image of a Stochastically Generated DFN with one hundred individual fractures in a domain of size of h × 20. Each color represents a different fracture in the network. The unconstrained network does not produce a high quality computational mesh without manual adjustments preformed in a post processing step.

Generally mesh generation requires some trade-offs in order to obtain a mesh that is optimal for a particular application. There are two competing issues. One is that it is desirable to keep the mesh as small as possible (minimize the number of vertices/cells) to keep computational costs down. The other is that the mesh cells must meet quality criteria since cell shape has an impact on the stability and accuracy of the physics solution being computed. In general these two criteria compete with one another. The exact definition of quality for a specific application must consider the demands of the physics code that is utilized. Because the target of this application is the FEHM code, there are two hard constraints that must be met. The FEHM discretization uses the Voronoi dual tessellation derived from a Delaunay triangulation (Delaunay 1934; de Berg et al. 2008). Therefore the triangulation of each fracture must be a Delaunay mesh. In addition, there is a requirement that all triangles with an edge on an exterior boundary must not be obtuse. Further details of the need for these criteria, how they can be met and the algorithms utilized are outlined in Murphy et al. (2001). Mesh quality can be measured using various metrics. The specific quality metrics used to characterize the meshes presented in this work are outlined further in the methodology section.

When meshing these complicated networks there exist some pathological cases that degrade mesh quality and must be addressed. One such case is the occurrence of a very small line of intersection between fractures. In order to resolve small features, the mesh must have edges that are less than or equal to the length of the feature. For arbitrarily small intersections, this requirement is computationally infeasible. Similarly, if an intersection is arbitrarily close the edge of one of the fractures the same issue arises. Another pathological case is the intersection of two arbitrarily close and parallel fractures with a third fracture. The mesh of the third fracture needs triangles small enough to cover the space between the two fractures. Other cases involve short lengths between multiple intersections, a high density of intersections on a fracture, and two fractures that are arbitrarily close to one another that do not intersect. All of these cases, and others not listed, cause features in the network that are very expensive to resolve and either drive down the quality of the mesh, introduces a very wide range of length scales of mesh edge lengths or increase the number of cells required to mesh the geometry.

In addition to the pathological cases, there exist other properties of the network that makes meshing a DFN difficult. Foremost, as the number of fractures in the network increases, the number of computational cells also grows linearly. Since the length of an intersection on an unconstrained stochastically generated DFN may be arbitrarily small, the difference in length scale between the smallest intersection and the largest fracture can be such that machine precision of coordinates becomes a problem. The mesh must be able to resolve all the features in the network and doing so efficiently across such a wide range is not trivial. Finally, the fractures ought be meshed in a manner that preserves the lines of intersection. Although conforming meshes are not necessary, as one can enforce continuity of pressure and flux on non-coinciding cells along fracture intersections, it greatly simplifies computations preformed on the network to have the meshes conform. In this context ‘conform’ implies that the line defined by two intersecting planar fractures is discretized as a set of line segments and these line segments exist as shared triangle edges in the triangulation of two intersecting planar fractures.

Many of the attempts to resolve the issues arising when meshing a DFN follow a similar trend. The methods generate a network of fractures stochastically, mesh the resulting network, and systematically move through the mesh removing or modifying vertices and edges that introduce undesirable pathologies. In a series of papers Mustapha, proposes a systematic method to generate a quality mesh in both two and three dimensions (Mustapha et al., 2009; Mustapha 2010; Mustapha et al., 2010). The procedure generates a DFN stochastically with given length scales, discretizes the edges of the fractures, and then meshes the network. To correct the poor quality mesh that arises due to short intersections and multiple intersections, a cube of length h systematically advances through the domain and removes undesirable features in the mesh by merging edges and eliminating vertices at problem locations. In the process of adjusting the mesh, the method also modifies the geometry of the network. Marška et al. (2004) suggests a method that moves, stretches and merges intersection to simplify the two-dimensional geometry. On the resulting meshes, the edges of neighboring cells are not geometrically identical; the only condition is that the outflow from one triangle has to be the inflow into the connected ones. Another method creates a conforming mesh by penalizing configurations stemming from close fractures and acute angles between fracture intersections Erhel et al. (2009). All of these methods modify the geometry and/or topology of the DFN during adjustment of the mesh. In most cases the adjustment of DFN is minor. Occasionally, however, the original structure is no longer represented in the mesh and while the input DFN is made up of planar fractures, the mesh representation may not be planar.

Another alternative bypasses the issue of resolving small features by not requiring the meshes of two fractures to coincide at the lines of intersection (Pichot et al. 2010). However, when using this method it is more difficult to implement the flow and transport and is more expensive computationally than having the meshes align.

2.4.1 Meshing Methodology

The existing methods to mesh a DFN outlined in the previous section modify an unconstrained stochastically generated DFN. Our method addresses the pathological cases listed previously during the generation of the DFN rather than afterwards. Our method defines a minimal feature size that will be resolved and any feature of the DFN less than this length scale is not represented.

Each fracture in our DFN is a planar straight-line graph (PSLG) made up of the set of line segments that represent the boundary of the fracture and the line segments that represent where other fractures intersect it (see Figure 2-4). There are three types of fracture intersections that are allowed to occur; intersections that are within the boundary of the convex polygon and do not have any vertices on the polygon boundary; intersections that cut the polygon into two regions and have two vertices on the polygon boundary; intersections that have one vertex on the polygon boundary and one vertex within the polygon. Multiple intersections are not allowed so the case of line segments that represent fracture intersection intersecting one another, if they occur, are removed.

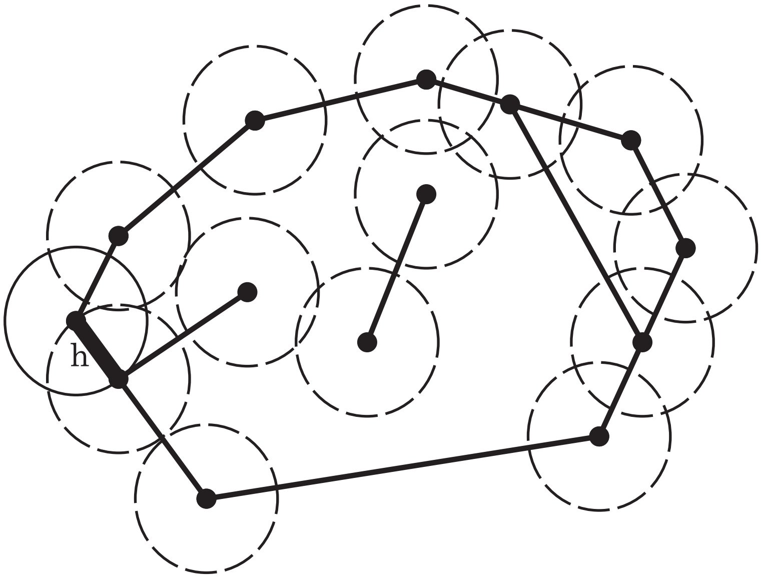

Figure 2-4. Vertices and line segments show the possible configurations of a planar straight line graph of fractures represented by convex polygons and fracture intersections that can have zero, one or two vertices on the polygon boundary. The minimum feature size *h* occurs on the heavy line segment on the left side of the polygon. All other features in the PSLG shown are larger than *h* as shown by circles of radius *h* centered on vertices of the PSLG. None of the dashed circles contain two or more vertices.

For a single PSLG, one can define a local feature size (Ruppert, 1995):

Given a PSLG *X*, the local feature size at a point *p*, is the radius of the smallest disk centered at *p* that intersects 2 non-incident vertices of segments of *X*.

We prescribe a length scale *h* and require that the stochastically generated DFN will never generate a fracture PSLG with feature less than *h*. Examples of features that must be larger than *h* are, the length of the line of intersection between two fractures, the distance from the polygon boundary to the end of a fracture intersection that is interior to the polygon, and the distance between two fracture intersection line segments. When the resulting network is meshed, all features are resolved by the using cell edges with a minimum length just slightly less than *h* and edges smaller than *h*/2 are never created. Away from intersections, where the smallest features exist, the mesh is coarsened to reduce the number of cells in the mesh.

This procedure eliminates arbitrarily small features that make it difficult to generate a high quality mesh. The physical basis for this is that when we develop a particular DFN model we make a decision as to the minimum size feature we choose to represent. That could be 1mm or 1km, but the DFN model will then reflect this choice.

In addition to the definition of feature size for a single two-dimensional PSLG, we extend the definition to three dimensions as:

Given a set of PSLGs *X* with arbitrary orientation in R^3, the local feature size at a point *p*, is the radius of the smallest sphere centered at *p* that intersects 2 nonincident vertices of segments of *X*.

Each fracture is represented as an *n*- vertex convex planar polygon. In this paper the fractures are restricted to rectangles and ellipses. However, the method is robust and can be applied to any general convex planar polygon.

The network is constructed one fracture at a time. Each new fracture is conditionally placed in the network. It is then checked to see if the new fracture generates a feature of length less than *h*. The new fracture is rejected if it does and kept if it does not. The algorithm for any given fracture F_i is listed below.

Create F_i with a given shape, orientation, and location in $R^{3.}$

Compute the minimum feature size created by the new fracture, h_i-*min*

If h_i-*min* > *h*, F_i is accepted into the set of fractures, else it is rejected.

The case when two fractures intersect on the surface of another fracture is also rejected due to the additional complications that an intersection of intersections causes. This choice to reject triple intersections is one of convenience in this initial implementation and does not represent a fundamental limitation of the approach.

After a specified number of fractures are generated, all isolated fractures are optionally removed because the intention is to compute flow and transport through the DFN and isolated fractures do not interact with the rest of the network. In more advanced applications where the space between fractures is also explicitly meshed, the isolated fractures may be retained.

Once the network is generated each fracture is meshed individually in a manner that preserves the polygon boundary and line segments corresponding to fracture/fracture intersections. The meshing is performed using the software LaGriT (Los Alamos Gridding Toolbox, 2011). When meshing each fracture PSLG a conforming Delaunay triangulation algorithm is used to insure that the line of intersection between any two fractures is preserved. The algorithm was presented and proven to be a sufficient condition for a conforming Delaunay triangulation in Murphy et al. (2001). The basic idea is that to ensure a Delaunay triangulation that preserves the lines of fracture intersections as a set of triangle edges, the circumscribed circle of each fracture edge must be empty (Figure 2-5).

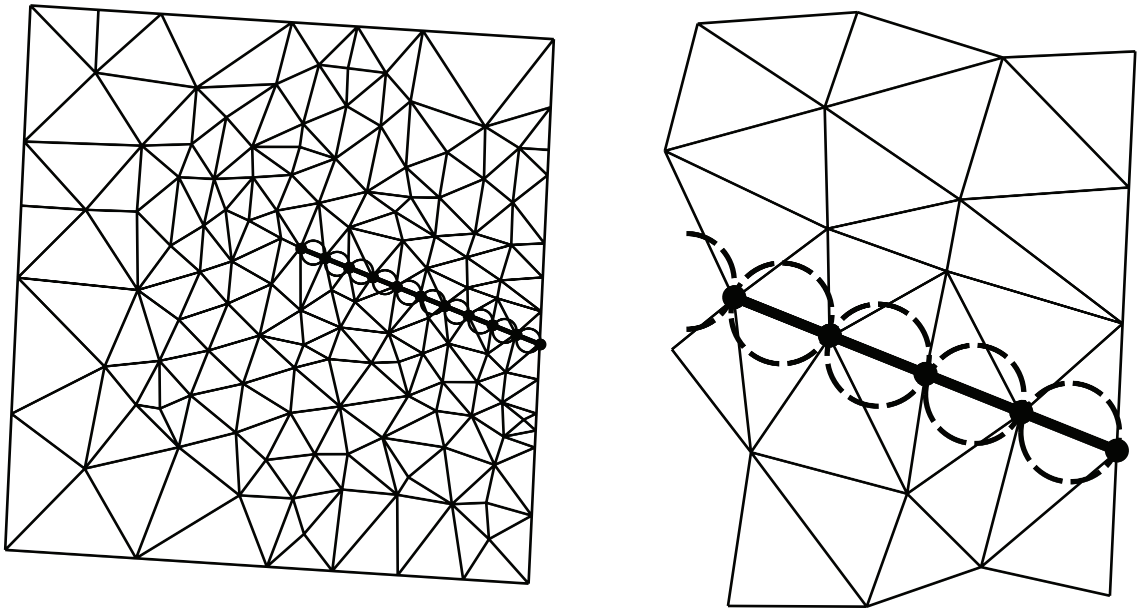

Figure 2-5. A conforming Delaunay triangulation of a rectangular fracture plane with a single fracture intersection segment that originates on the exterior boundary and terminates in the interior. The line segments that represent the fracture intersection are preserved by ensuring that the circumscribed disk of each line segment does not contain any vertices of the triangulation.

In order that the meshes on intersecting fractures align at the intersection, the points on the discretized line of intersection are constructed to coincide on the two individual fractures. Since computational control volumes (Voronoi polygons) are based on vertices and the triangular meshes are coincident at the intersection, the Voronoi cells also conform at the fracture boundaries. At fracture intersections, the control volumes are three-dimensional objects resulting from the union of two two-dimensional Voronoi cells; one cell lies in each of the intersecting fracture planes (Figure 2-6). Away from the intersections, each control volume Voronoi cell is two-dimensional.

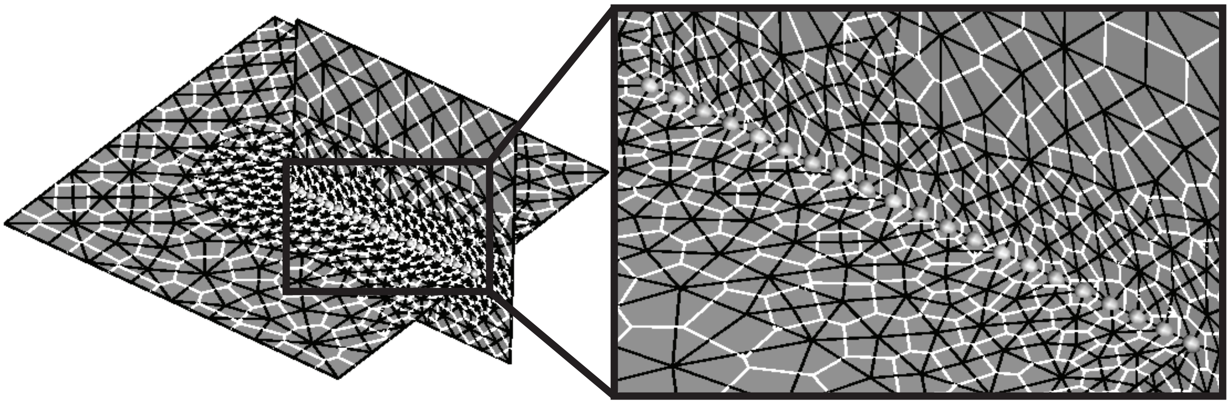

Figure 2-6. A fully meshed set of two fractures. The black lines are the Delaunay triangulation, the white lines are the Voronoi Cells, and the white spheres marking vertices are common to the intersecting fractures. The resulting Voronoi cells are two-dimensional away from the fracture intersections. At the fracture intersections the control volume cells are three-dimensional and result from the merging of two two-dimensional Voronoi cells.

Because the physical processes that occur at intersections between two fractures will result in the largest gradients in physical parameters, we optionally refine the mesh near the intersection below the length scale *h* so features of length *h* are adequately resolved. As the distance from intersections increases the mesh is coarsened in order that computational resources are not expended in areas with low gradients.

After all the fractures have been meshed individually, they are merged to create a single fully meshed three-dimensional fracture network.

2.4.2 Example DFNs

Figure 2-7 explicitly shows the conforming mesh of a single fracture. This particular fracture intersects with four other fractures. The lines of intersection are represented in the mesh by colored vertices. Notice how the mesh conforms to the intersections and does not deform the fracture or the line of intersection.

Figure 2-8 highlights the quality of the meshes that the proposed method generates. The intersection vertices, shown as green dots, and triangle edges along the line of intersection between the two is coincident. Hence the triangulations on of each fracture aligns with the other fracture. The Voronoi control volumes on each of fractures is displayed on the right side of the figure. The Voronoi cells corresponding the green vertices are on both of the fractures. Notice, the neighbors of these Voronoi cells are still two-dimensional. Finally, notice that the mesh gradually coarsens away from the line of intersection.

Figure 2-9 shows the complexity of the fully meshed DFN and how the proposed method is capable of resolving the issues mentioned previously. At the lines of intersection the mesh is refined. The mesh is coarsened away from the fracture intersections. Notice that the method is capable of meshing fractures with an arbitrary number of intersections as long as the minimum feature size criterion is met.

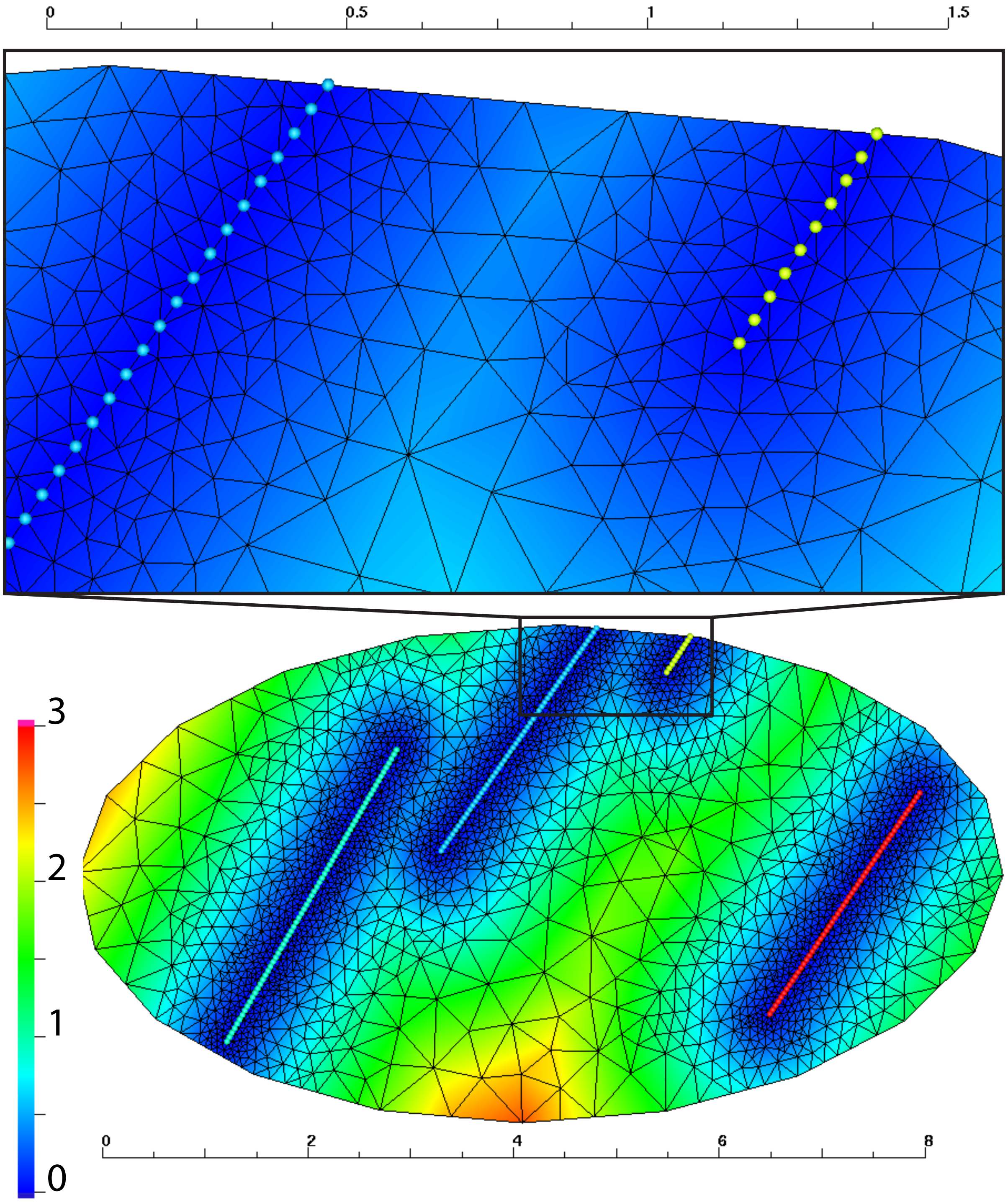

Figure 2-7. A fully meshed Single Fracture with conforming Delaunay Triangulation to lines of intersection. The field color represents distance from the nearest line of intersection. Each line of fracture intersection is highlighted in a different color. In the magnified view vertices that fall on the fracture intersection lines are plotted as dots. The lines of intersection are represented in the mesh and the fracture has not been deformed to ensure their inclusion. The mesh has been optionally coarsened away from the intersections to preserve computational resources.

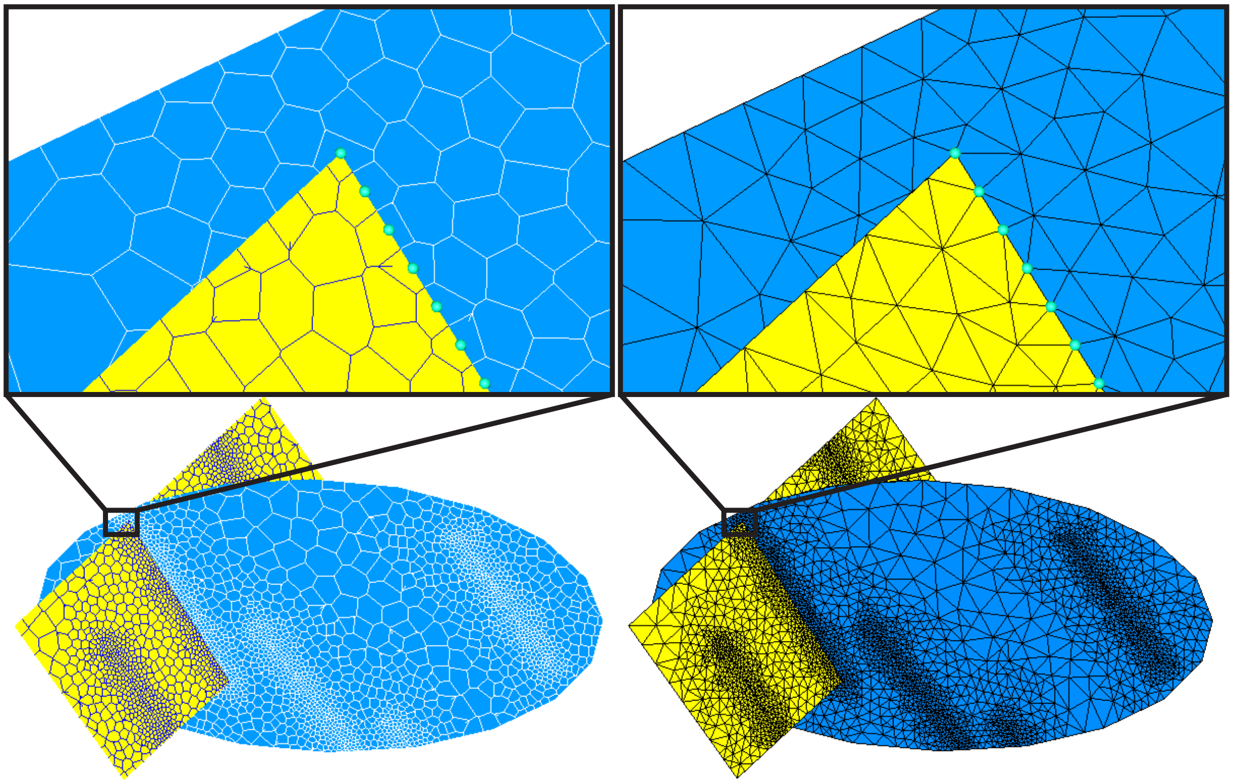

Figure 2-8. Two fractures showing the intersection conforming Delaunay triangulations (right) and Voronoi control volumes (left). Notice the Delaunay triangularization conforms to the intersection of the fractures without distorting either the lines of intersection of the fracture geometry. The triangles in the mesh coincide along the intersection. Along the line of intersection the Voronoi cells are common to both fractures.

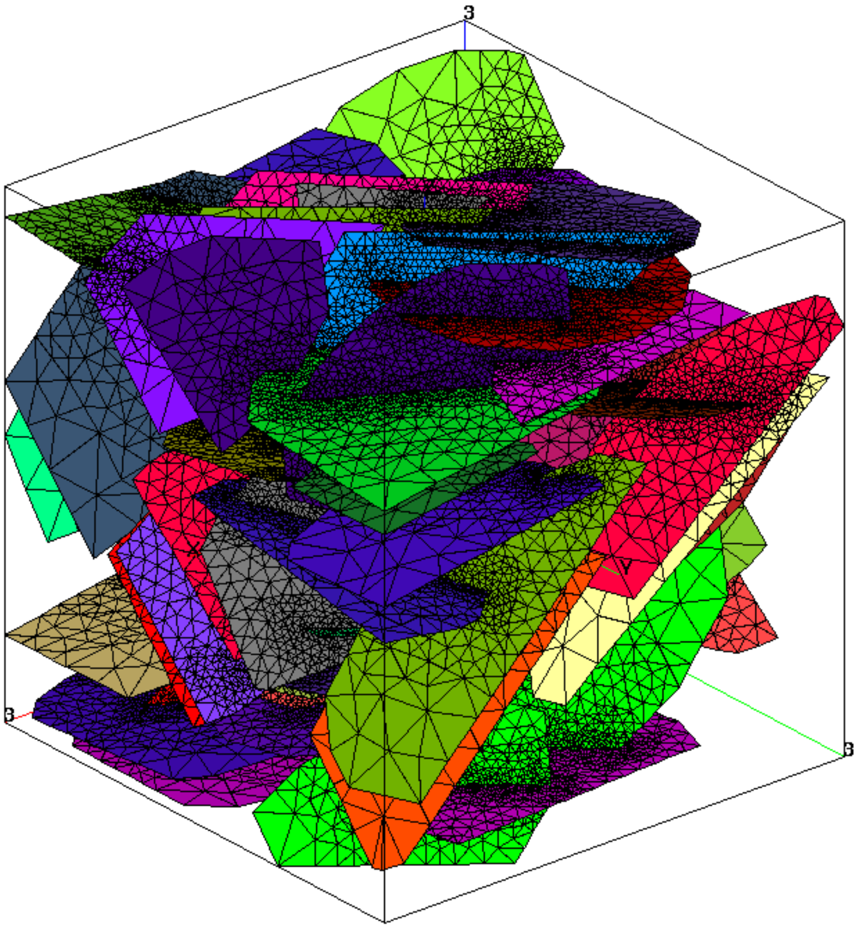

Figure 2-9. Fully meshed 100-fracture network of ellipses highlights the variable mesh resolution. The mesh is fine near fracture intersections and coarse away from fracture intersections. The domain size is h × 50. Each color represents an individual fracture. The constraint that no feature exists in the network less than h guarantees that the mesh will not have an arbitrarily small edge and that no manually adjustments to either the network or the mesh need to be deformed in a post-processing step.

2.4.3 Network Statistics

In order to exemplify the quality of the meshes generated by the proposed method, ten different networks of approximately one hundred fractures apiece are generated and meshed. All of the networks are made of ellipses described by twelve vertices, drawn from two fracture sets with different mean length, orientation, and aspect ratio. Certain properties used in the generation of the networks are varied including: the perturbation of the normal vectors of each fracture set, the aspect ratios of the ellipses, and the mean and standard deviation of the distributions from which the length of the fractures are sampled. In some cases the normal vectors of the fractures sets are orthogonal, in some cases they are not. The fractures range in length from *O(1) m* to *O(10) m*. The same minimum length scale *h* is used for all of the networks, 0.1 *m*. The combination of all the networks results in roughly 5×10^6 triangles.

A standard metric of mesh quality is the aspect ratio of its triangles. The aspect ratio is the ratio of the radius of the circumcircle of a triangle over twice the radius of its inscribed circle. Figure 2-10 is a histogram of the aspect ratios for all ten networks. Of the approximately 5 $\times 10^6$ triangles in the sample set 99.6% have aspect ratios between 0.5 and 1. Not only are the majority of the aspect ratios greater than 0.5, but 55% are greater than 0.9. Another test of quality for a mesh is the edge ratio, which is the ratio of the minimum edge length over the maximum edges length. Figure 2-11 shows that edge ratio for the same network. This histogram shows that 98% of the triangles have a min/max edge length ratio greater than 0.5. Figures 2-12 and 2-13 are histograms of the minimum angle of the triangles and the maximum angle. Notice that they are both close to the ideal angle for equilateral triangles of 60 degrees. Note that there is a spike in the maximum angle at 90 degrees. This is because a mesh modification step is applied for numerical accuracy that ensures that no triangle circumcenters fall outside the polygon boundary. This is accomplished by splitting any boundary triangle with an angle incident on the exterior boundary greater than 90 degrees. The algorithm to accomplish this is described in Murphy et al. (2001).

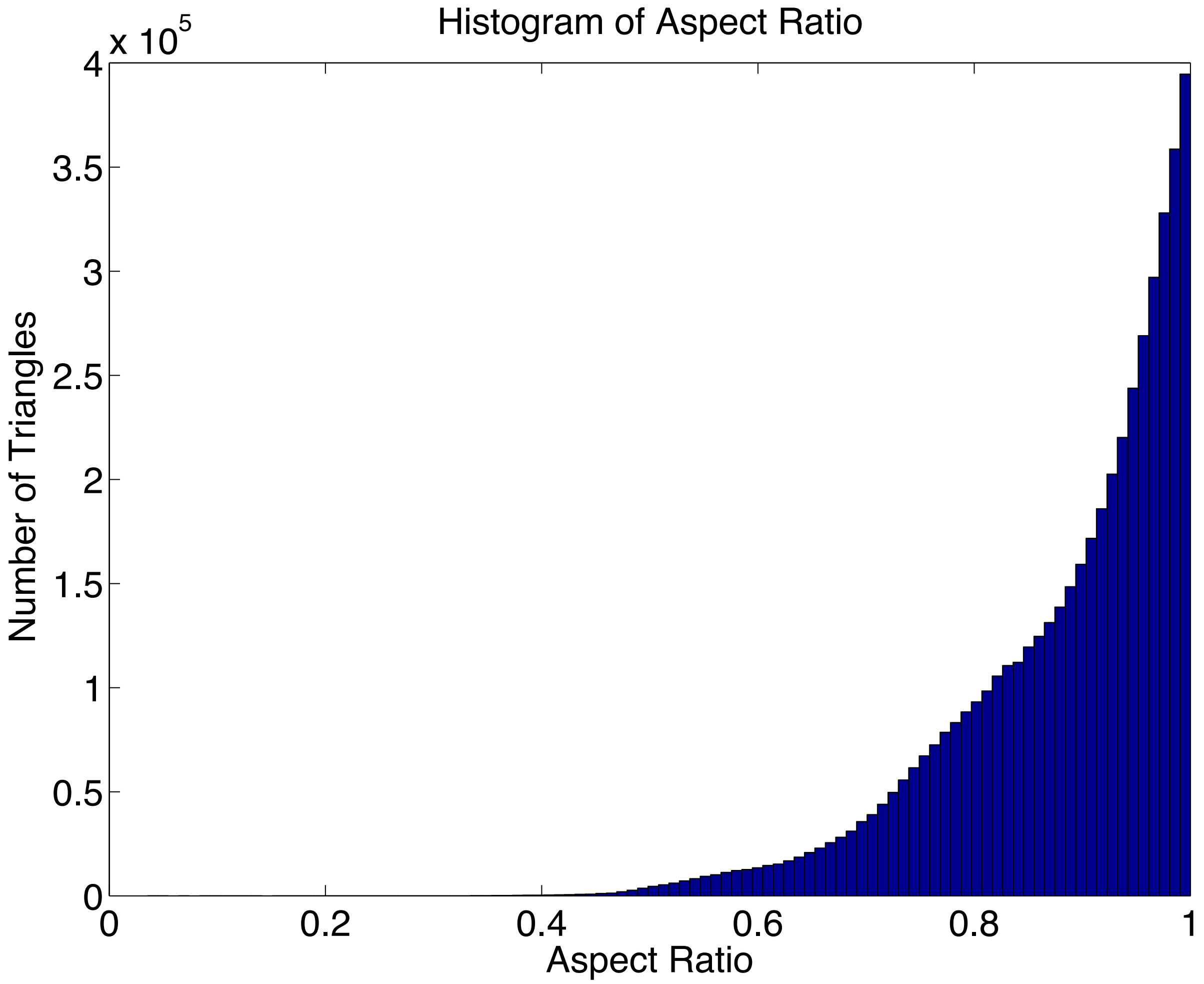

Figure 2-10. Histogram of triangle aspect ratios in grids generated from 10 DFN realizations with 100 fractures in each realization.

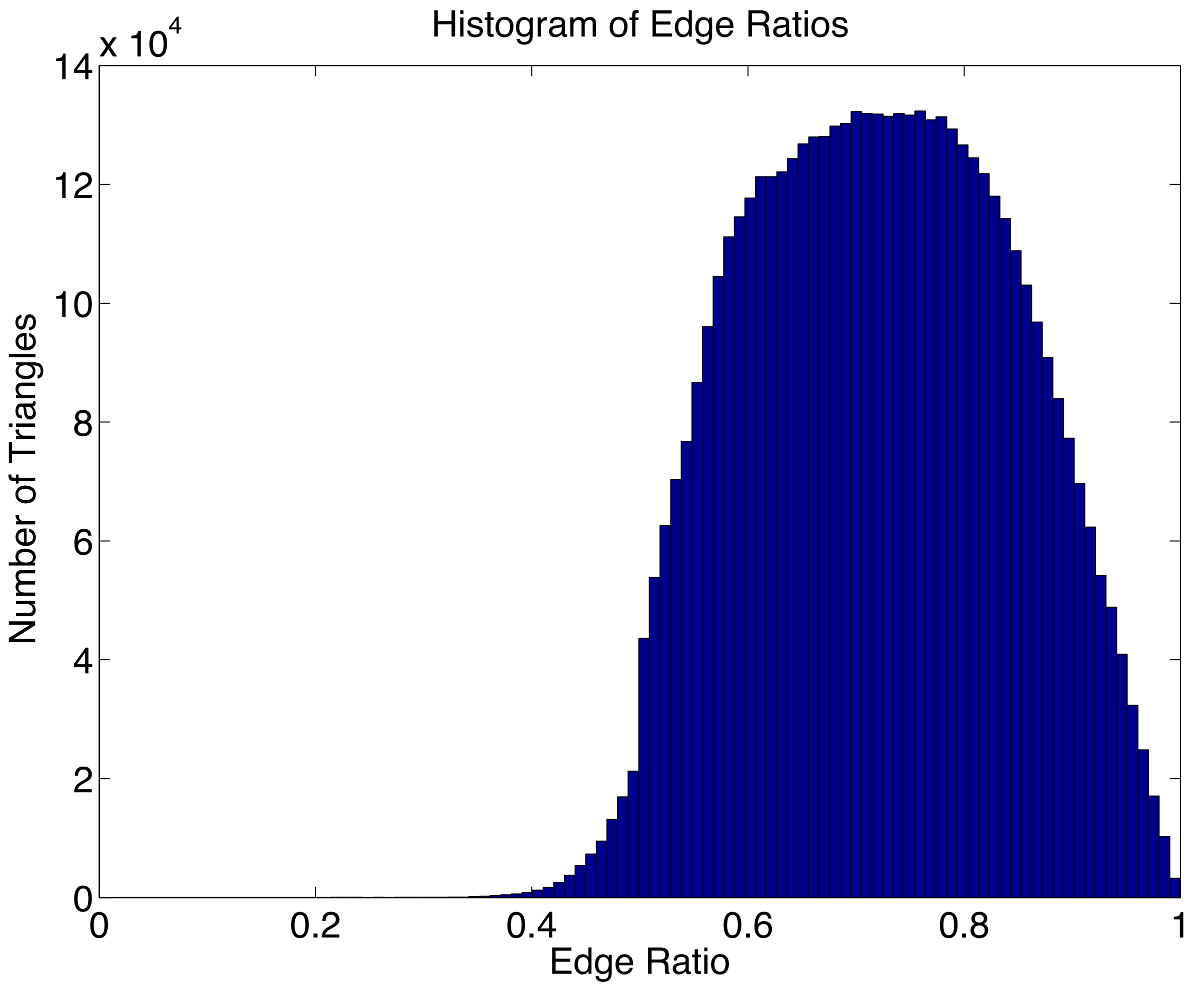

Figure 2-11. Histogram of triangle edge ratios in grids generated from 10 DFN realizations with 100 fractures in each realization.

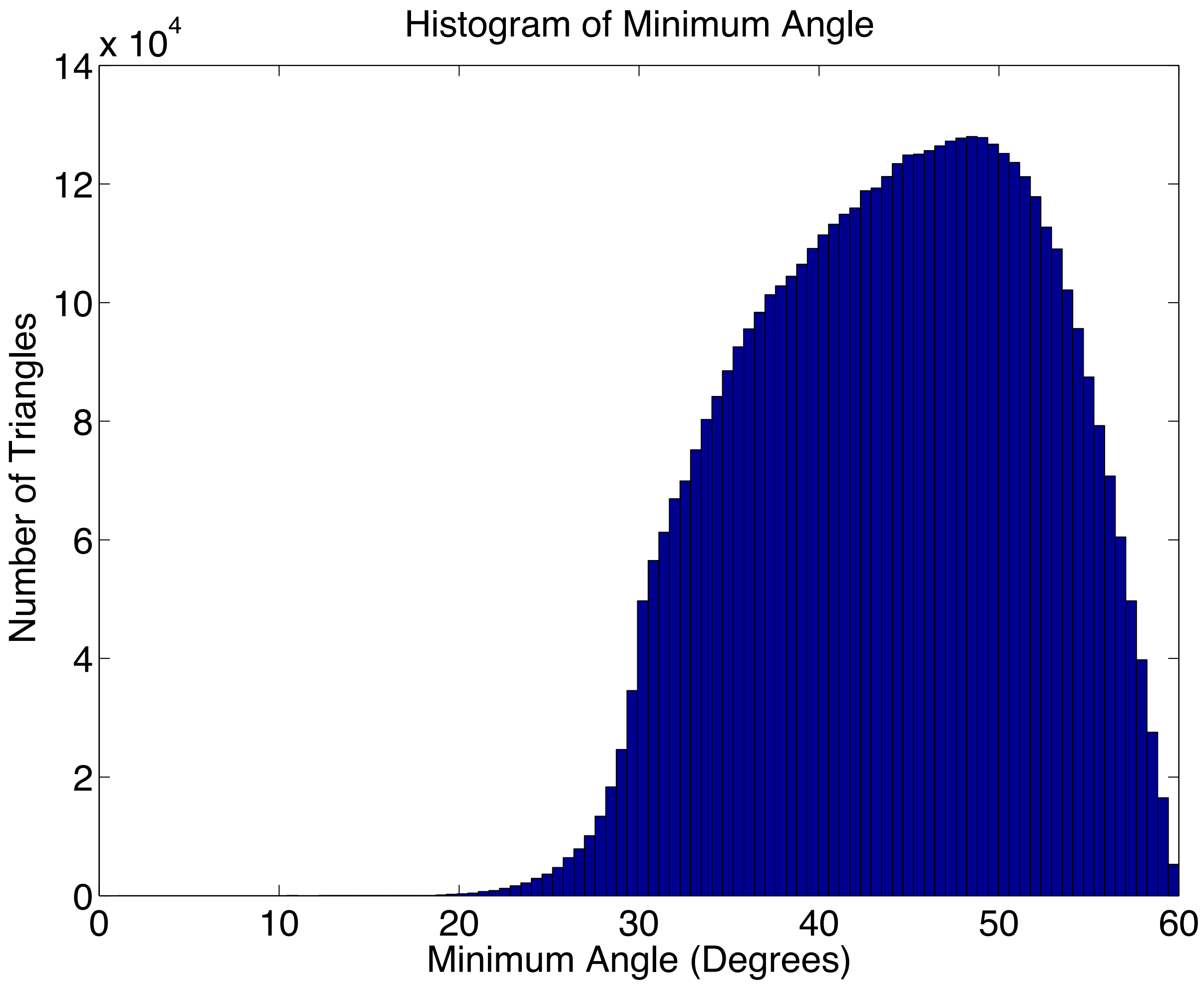

Figure 2-12. Histogram of minimum angle in grids generated from 10 DFN realizations with 100 fractures in each realization.

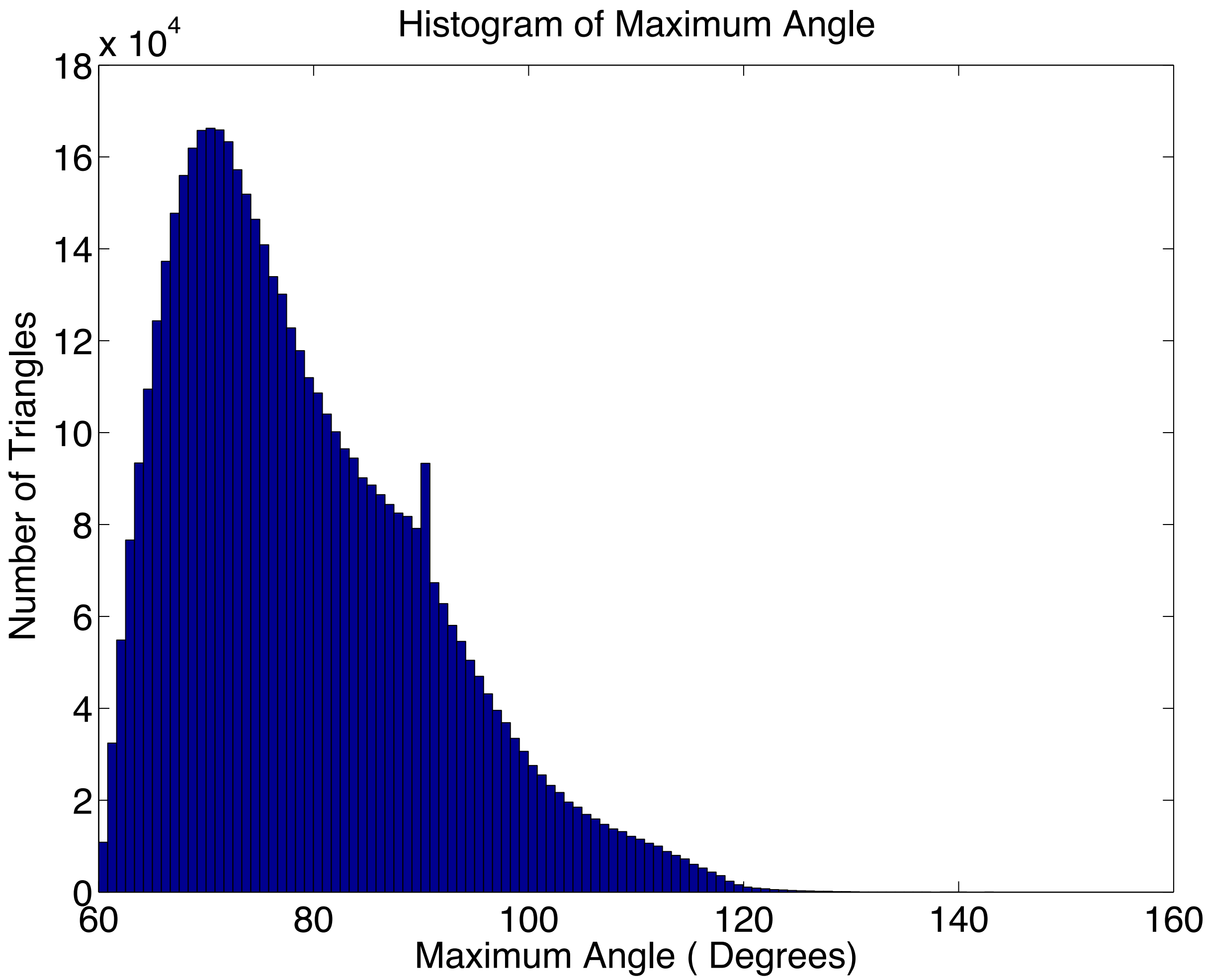

Figure 2-13. Histogram of maximum angle in grids generated from 10 DFN realizations with 100 fractures in each realization.

2.4.4 Example Flow Solution

An example flow pressure solution resulting from the method described here is shown in Figure 2-14. In this example, constant pressure boundary conditions were applied to the x-faces of the 5 m × 5 m × 5 m box and the FEHM code (Zyvoloski, 2007) was used to obtain steady-state pressure on the 100-fracture network. The left image of Figure 2-14 shows the pressure field for the entire network with warm colors representing high pressures. The right image shows a detail from the pressure solution with the computational grid superimposed. This calculation demonstrates the practical utility of the new approach for use in groundwater flow simulations.

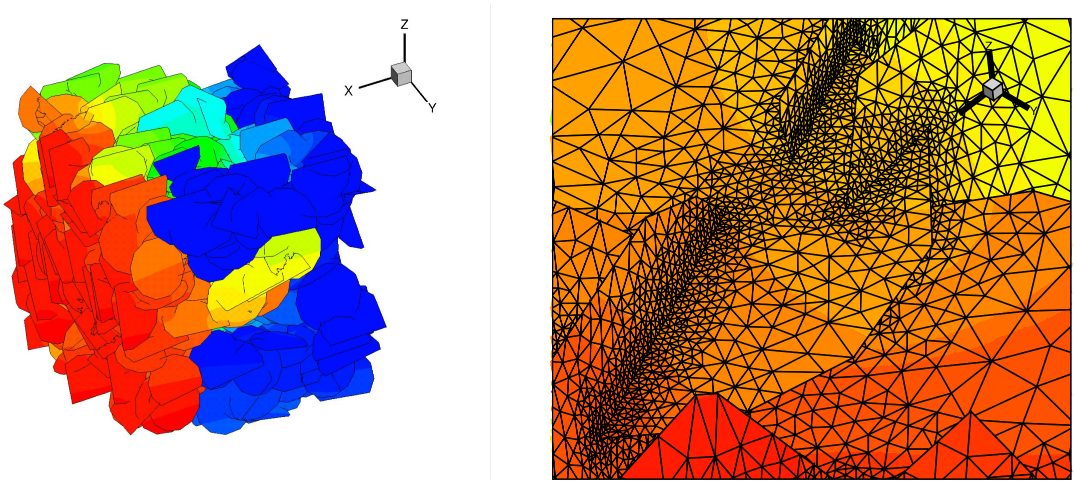

Figure 2-14. Example pressure solution solved on the Voronoi control volumes dual to a Delaunay triangulation generated on a DFN. The FEHM flow code was used to obtain the pressure solution. Warm colors represent high pressures. Smooth and directionally unbiased solutions result from the finite volume code due to the high quality of the mesh resulting from the constrained network.

2.5 Particle Tracking on DFNs

2.5.1 Reconstruction of the Velocity Field

Particle tracking requires the flow velocity and dispersion tensor at all points in the simulation domain. Velocity (and by extension dispersion tensors) is explicitly available in a mixed hybrid finite element solution to flow; particle tracking is relatively straightforward in this case. Particle tracking using flow solutions obtained on unstructured control volume grids is more problematic. Specifically, the control volume flow solution does not provide the continuous velocity field. Instead, it provides a set of scalar quantities that are approximations to the normal component of the darcy flux integrated over each face of each control volume (in two-dimension, each control "volume" is a polygon and each "face" is one line segment on the perimeter of the polygon). If particle tracking is to be used on an unstructured control volume, it is necessary to reconstruct a continuous velocity field from these scalar quantities. There is no unique solution to this reconstruction problem and, as far as we are aware, no general method in the literature.

A new method for particle tracking using flow solutions obtained on unstructured control volume grids has been developed (Painter et al. 2011) and is currently being tested for use in DFN transport simulations. The method works on a subset of finite volume methods where each fracture has been partitioned into control volumes (polygons) formed by perpendicular bisectors between adjacent nodes in an underlying triangulation of cell centers. Specifically, a nodal network triangulated into a triangular element mesh is presumed to be available. A control volume V_i is constructed around each node *i* in the triangulation such that V_i is bounded by the set of perpendicular bisectors between node *i* and each of its neighbors. Note that this approach makes no assumption about the shape of the finite volume cell. It is further assumed that a control-volume method with 2-point flux approximation has been used to solve for groundwater head. Specifically, the conservation equation is written for a control volume V_i as

$$S_i |V_i| \frac{\partial h_i}{\partial t} = \sum_{j \in N(i)} Q_{ij} \qquad (2\text{-}1)$$

where S_i, h_i and $|V_i|$ are the specific storage [L^{-1}], head [L] and volume [L^3] in cell *i*, respectively. Here *N(i)* is the list of neighbors adjacent to cell *i*, $Q_{ij} \equiv \int_{V_i \cap V_j} \mathbf{q} \cdot \mathbf{n}_{ij}\, ds$ is volumetric flow rate [L^3/T] through the face connecting cells *i* and *j*, and $\mathbf{n}_{ij}$ is the unit normal on the same face.

Our interest is in the velocity vector $\mathbf{v} = \mathbf{q}/\phi$ in the entire domain. However, the flow solution only provides the Q_{ij}, the normal components of **q** at each cell face. The approach proposed and tested here has two steps. In the first step, the Q_{ij} for each cell are used to construct an approximate representative value of **q** for that cell (denoted $\mathbf{q}_i$, for cell *i*). Second, the $\mathbf{q}_i$ are then associated with the nodes and the original triangulation is then used to interpolate to any point in the computational domain.

The first step is to reconstruct cell-centered velocities. To this end, **q** is (temporarily) approximated as being constant in each cell. The volumetric flow rate across the face common to cells *i* and *j* then becomes $Q_{ij} = \mathbf{q}_i \cdot \mathbf{A}_{ij}$ where $\mathbf{A}_{ij} \equiv A_{ij}\mathbf{n}_{ij}$ is the vector area for the face. An analogous equation can be written for each face on the cell, thus producing the linear system for each cell *i*

$$\mathbf{G}_i \mathbf{q}_i = \boldsymbol{\gamma}_i \qquad (2\text{-}2)$$

Here $\mathbf{G}_i$ is a $n_i \times d$ matrix, $\mathbf{q}_i$ is $d \times 1$, and γ_i is $n_i \times 1$, n_i is number of neighbors for cell *i,* and *d* is dimensionality of the space. Each row of the $\mathbf{G}_i$ matrix is the vector area for one face. The columns vector $\boldsymbol{\gamma}_i$ is the volumetric flow rate across the faces, as calculated by the control volume flow code. The column vector $\mathbf{q}_i$, the darcy flux for the cell, is the unknown.

In two dimensions, a control volume has a minimum of 3 sides and in many applications involving an unstructured grid will have more. Similarly, a control volume in 3-D has 4 or more sides. Thus, equation 4 is an $n_i \times d$ system with $n_i > d$; i.e. it is an overdetermined system. Following standard techniques, a least-squares estimate $\hat{\mathbf{q}}_i$ can be constructed for the darcy velocity $\mathbf{q}_i$

$$\hat{\mathbf{q}}_i = \left(\mathbf{G}^{\mathrm{T}}\mathbf{G}\right)^{-1}\mathbf{G}^{\mathrm{T}}\boldsymbol{\gamma} \tag{2-3}$$

where the subscript i on $\mathbf{G}$ and γ has been suppressed for readability. An estimate of the velocity for the cell is then obtained as $\hat{\mathbf{v}}_i = \frac{\hat{\mathbf{q}}_i}{\phi}$ where ϕ is porosity in the cell.

For the types of grids considered here, nodes are specified on the domain boundaries. For nodes on Dirichlet boundaries, Equation 5 can be applied as for interior nodes. For nodes on Neumann type boundaries, the specified flux constraint must be included, which leads to a linearly constrained linear least squares problem for the boundary flux vector $\hat{\mathbf{q}}_i^b$ in the i-th cell

$$\hat{\mathbf{q}}_i^b = \arg\min_{\mathbf{q}_i} \left\| \mathbf{G}\,\mathbf{q}_i - \boldsymbol{\gamma} \right\| \quad \text{subject to } \mathbf{B}\mathbf{q}_i = \boldsymbol{\beta} \tag{2-4}$$

where $\mathbf{B}$ is a $n_i^b \times d$ matrix, and β is $n_i^b \times 1$; $n_i^b < d$ is the number of boundary faces for the cell in question. The matrix $\mathbf{B}$ and the column vector $\boldsymbol{\beta}$ are analogous to $\mathbf{G}$ and $\boldsymbol{\gamma}$ but are written for the subset of faces for the cell in question that lie on the boundary. Explicit solutions are available (e.g. Amemiya, 1985)

$$\hat{\mathbf{q}}_i^b = \hat{\mathbf{q}}_i - \left(\mathbf{G}^{\mathrm{T}}\mathbf{G}\right)^{-1}\mathbf{B}\left(\mathbf{B}^{\mathrm{T}}\left(\mathbf{G}^{\mathrm{T}}\mathbf{G}\right)^{-1}\mathbf{B}\right)^{-1}\left(\mathbf{B}\hat{\mathbf{q}}_i - \boldsymbol{\beta}\right) \tag{2-5}$$

with Equation (2-3) for $\hat{\mathbf{q}}_i$. In the event that $n_i^b = d$ (i.e. for nodes at the corners of the domain) the boundary conditions alone determine the nodal velocities.

Quantitative tests of the velocity reconstruction method can be found in Painter et al. (2011).

In the DFN representation used here, a complicated non-uniform structure is used for the computational mesh. Nodes, as one of basic elements of a computational mesh, have different features and are classified to four different types (Figure 2-15):

Interior node is a node located inside a fracture. It does not belong to boundary or intersecting line. Velocity of interior node is represented by one velocity vector calculated by Equation 2-3.

Exterior node is a node located on a fracture's boundary. Velocity vector of exterior node is defined by equation 2-5. In a case when exterior node represents a corner the velocity vector is set to be zero for angle of a corner less than 90°. This helps to avoid undesirable stagnant point on a boundary of fracture.

Interior interface node is a node located on an intersection line of two fractures. It is an interior node that belongs to both intersecting fractures at the same time. Two velocity vectors are represented on interior interface nodes, one in each fracture. Equation 2-3 is used to calculate velocity for each intersecting fracture (Figure 2-15, zooming figure).

Exterior interface node is a node that belongs to an intersection and also lies on a boundary of one (or both) intersecting fractures. In this case the velocity is calculated by Equation 2-3 for flow in the fracture where the node is interior, and Equation 2-5 for flow in fracture were the node lies on its boundary.

Figure 2-15 shows the example of simple DFN that consists of 3 fractures only. The zooming figure shows an intersecting line (dotted line), where all interface nodes are interior nodes with two velocity vectors represented. The next step for higher accuracy of Darcy velocity reconstruction on fracture's intersections will be to separate control volume cell of each fracture onto two subcells, where each subcell is located on opposite side of intersection line. This method will give 2 velocity values on interface nodes in each intersecting fracture.

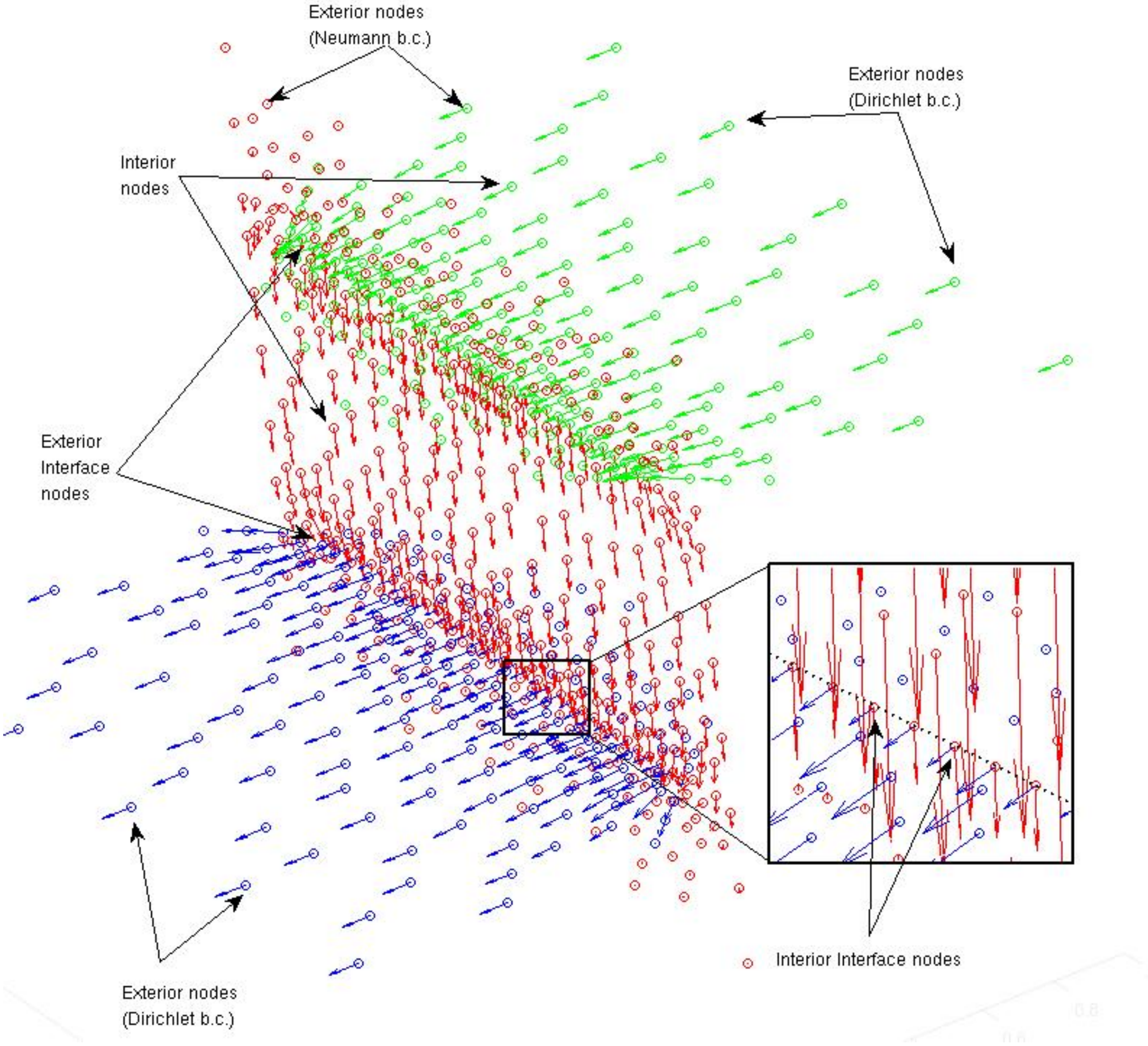

Figure 2-15. Reconstructed velocity field on a discrete fracture network consisting of 3 fractures in a 3D domain. Four types of nodes are indicated. Interface nodes have two velocity vectors represented, one on each fracture plane, as shown in the zooming frame.

2.5.2 Examples of Reconstructed Velocity Fields

Figures 2-16 and 2-17 show example velocity and pressure fields on individual fractures extracted from a 100-fracture DFN. Another example of DFN that consists of 10 fractures is shown in 3D in Figure 2-18.

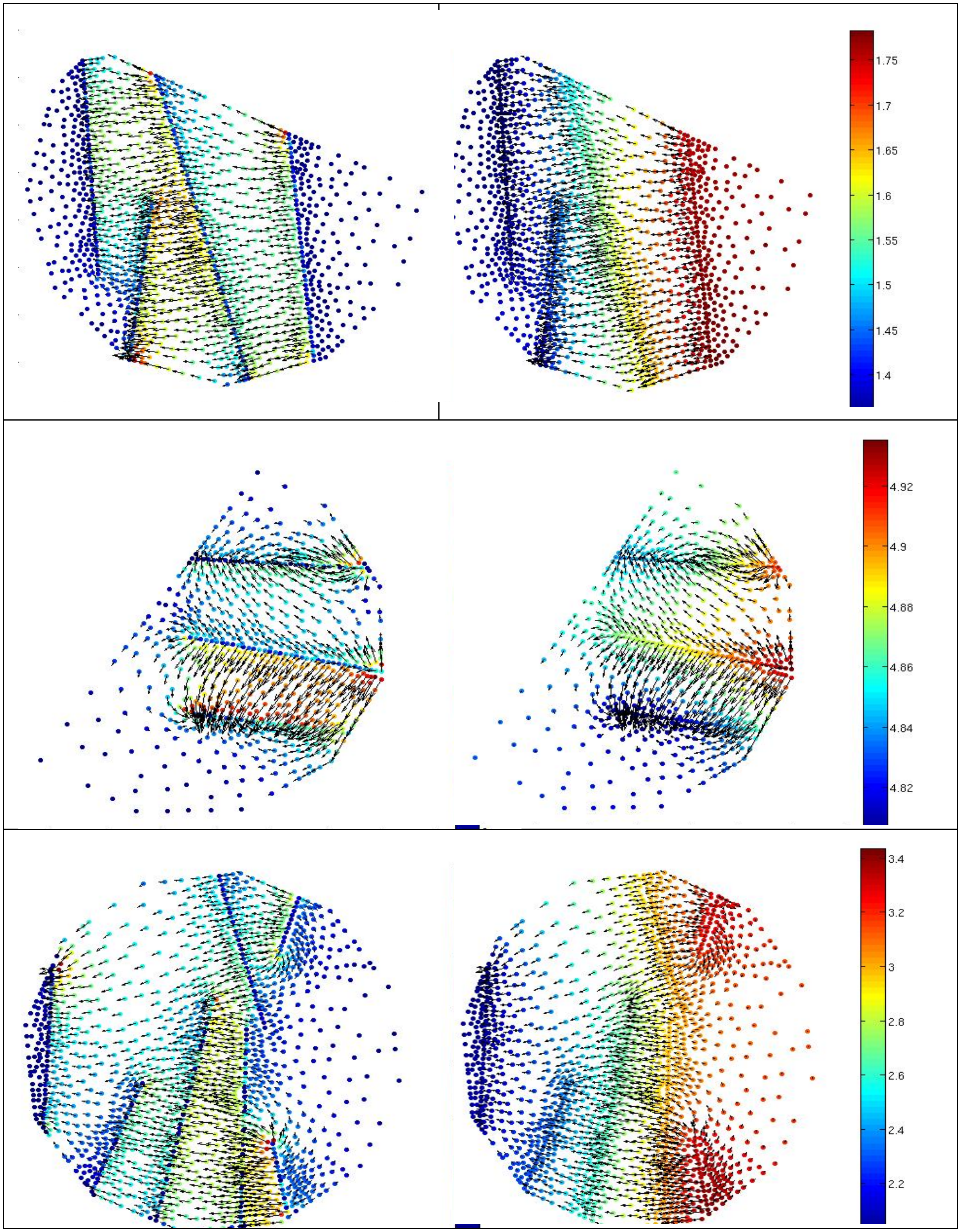

Figure 2-16. Velocity (left) and pressure (right) fields from three 2D fractures extracted from a 3D domain. The arrow at every node shows the direction of flow velocity. The magnitude velocities are shown by color on left panels. Liquid pressure [MPa] values on nodes, defined by flow solution, are shown by color on the right panels. In all cases, the warm colors represent high values.

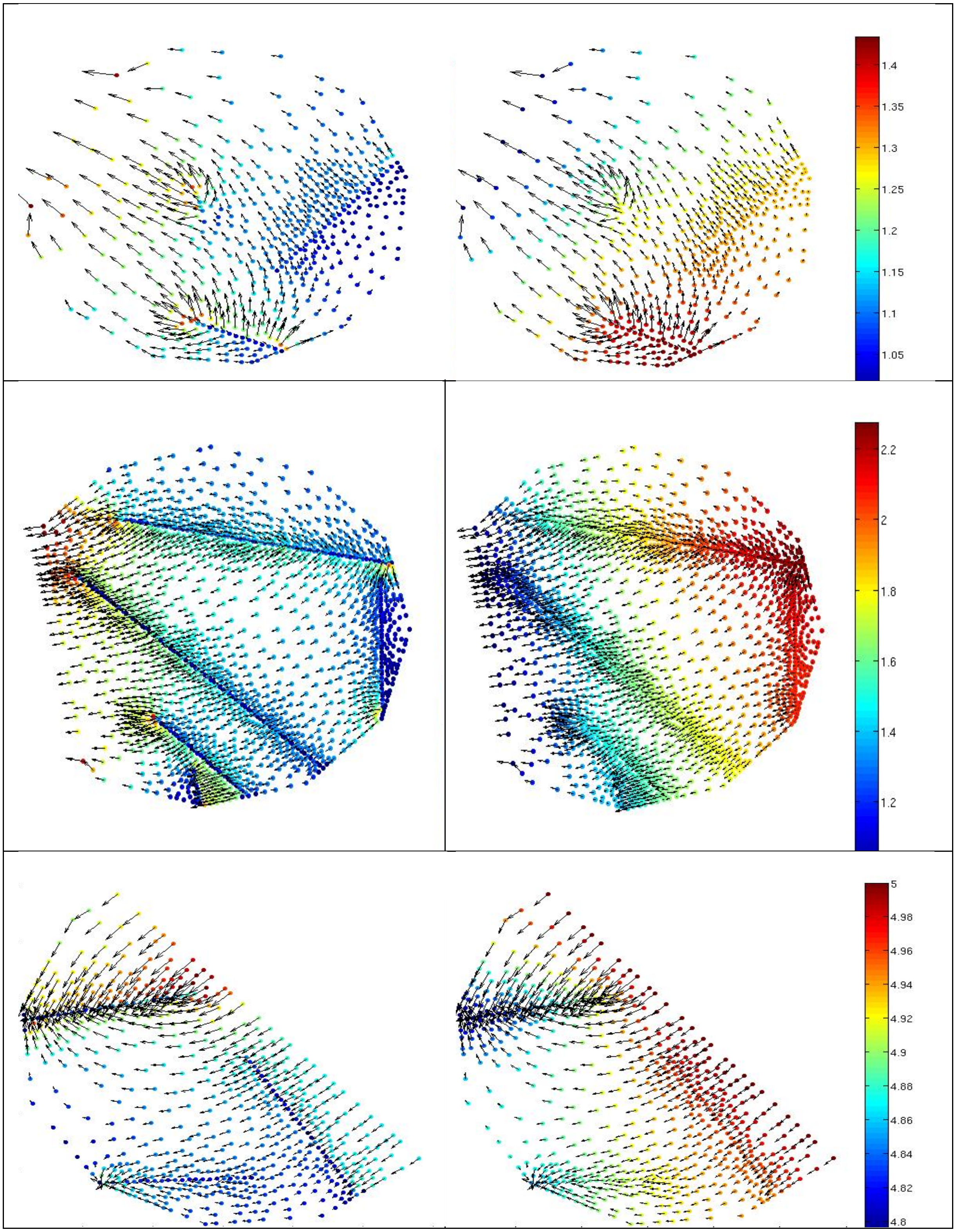

Figure 2-17. Same as Figure 2-16, but for three different fractures. Each of these fractures intersects a Dirchlet boundary of the domain.

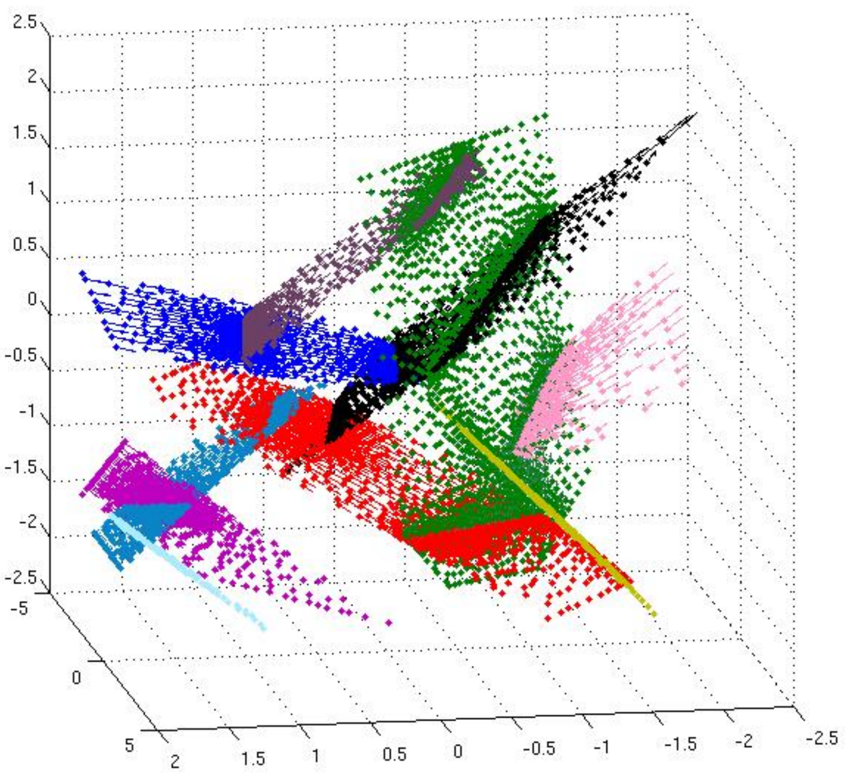

Figure 2-18. A DFN with 10 planar fractures. Arrows show flow direction that goes from left to right side of the domain.

2.5.3 Velocity Interpolation and Flow Streamlines

Velocities $\boldsymbol{v}$ at the nodal position in the computational grid, are used for determining the particle's velocity. At any computational time particle's position can be at any point inside domain, then its velocity value is defined using interpolation procedure. Here the standard barycentric interpolation approach is applied. In planar two dimensional space, if $\boldsymbol{r}_1$, $\boldsymbol{r}_2$, and $\boldsymbol{r}_3$ are the positions of nodes of the triangular cell (where particle is locate at current time step) and $\boldsymbol{v}_1$, $\boldsymbol{v}_2$ and $\boldsymbol{v}_3$ are the values of velocity at the nodes, the velocity of particle $\boldsymbol{v}_p$ at some point $\boldsymbol{r}$ in the triangle can be interpolated as

$$\mathbf{v}(\mathbf{r}) = \sum_{i=1,4} \lambda_i \mathbf{v}_i \qquad (2\text{-}6)$$

where

$\begin{pmatrix}\lambda_1\\ \lambda_2\\ \lambda_3\end{pmatrix} = \mathbf{T}^{-1}\left(\mathbf{r}-\mathbf{r}_4\right)$	(2-7)

$\sum_{i=1,4}\lambda_i = 1$ and **T** is the 3 × 3 matrix that has $\mathbf{r}_1$-$\mathbf{r}_4$ as the first column, $\mathbf{r}_2$-$\mathbf{r}_4$ as the second column and $\mathbf{r}_3$-$\mathbf{r}_4$ as the third column. Note also that derivatives of the velocity, which are needed to properly calculate dispersion tensors in a random walk particle-tracking model, are readily available from the interpolation.

Interpolated velocities are schematically shown in Figure 2-19, where particle travels on planar fracture with new positions at every time step are defined by Euler's method.

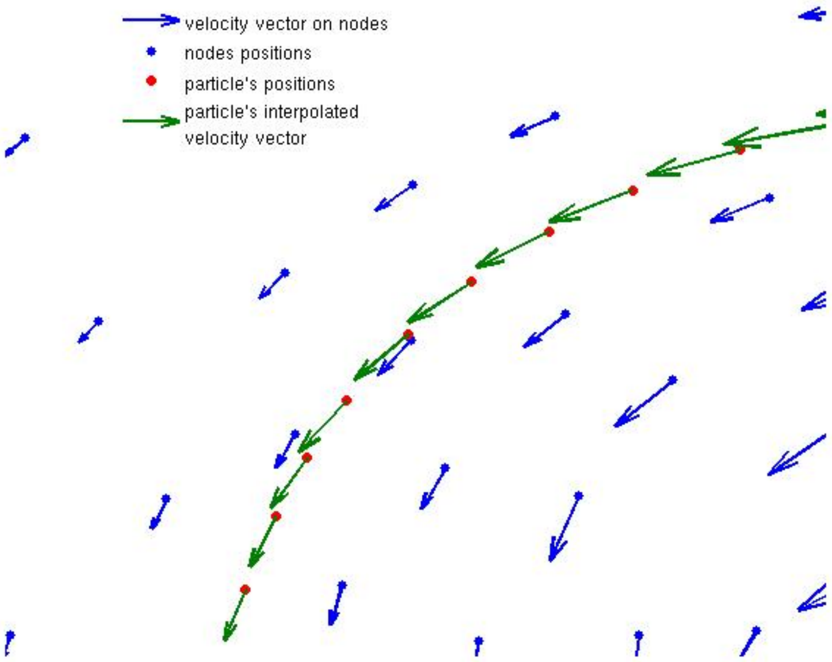

Figure 2-19. A fragment of particle's trajectory on a planar fracture. At every time step the particle's velocity is interpolated from the nodes that form a current cell.

Once the particle's velocity is known the particle can be tracked on a single fracture and a streamline can be defined. Figure 2-20 shows a few examples of streamlines, where particle starts from cells close to boundary and travels until it has been stopped at intersection line (top panel). Particle also can travel very close to fracture's boundary (beige line on bottom panel). It is shown that the streamline trajectories (inside a fracture and close to fracture's boundary) coincide with the flow direction.

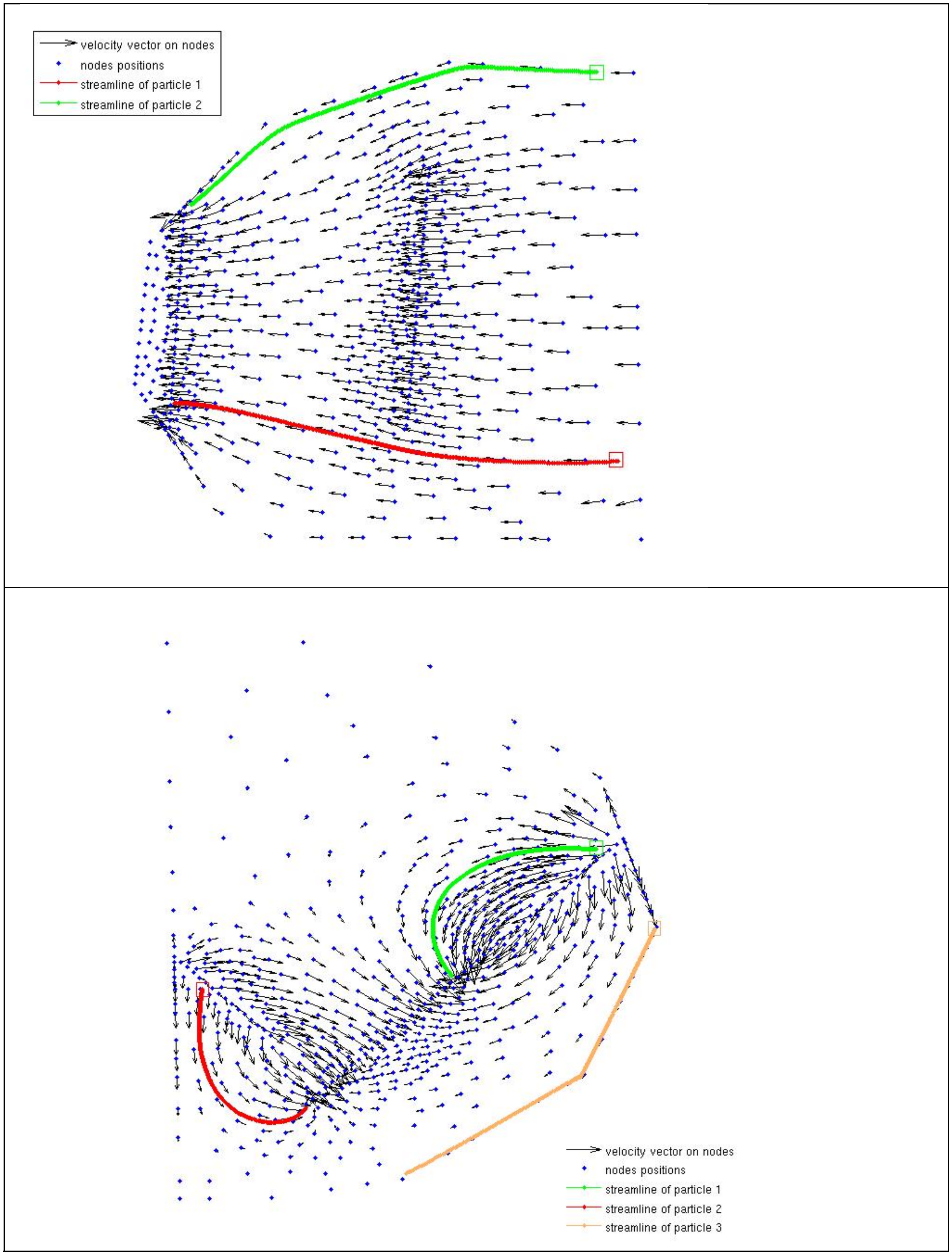

Figure 2-20. Two planar fractures with example streamlines. Particle starts at a point inside domain (starting location is shown by a rectangle).

2.6 Status and Plans for Future Work

There are two overarching motivations for this work on DFN modeling tools. First, the tools under development will be necessary should the UFDC be asked to evaluate a potential future site in fractured rock. Second, there are several unresolved generic scientific issues associated with flow and transport in fractured rock that these tools will be able to address. Of the component pieces of the work, the generation of a high-quality DFN computational mesh is largely complete for situation where the space between fractures is not meshed. Additional work is required to develop meshing capability for the spaces between fractures. The ability to generate flow solutions from the computational meshes is available for DFNs of relatively small size. However, additional work is needed to provide parallel high-performance computing flow modeling capability, thereby enabling larger networks. The particle tracking capability described here is at the prototyping stage and additional work is required to finalize that work. Finally, an important next step is to use these tools to model a few sites to develop the required knowledge base for full field scale deployment.

3. NON-NEWTONIAN FLOW IN CLAYS

3.1 Introduction

Water flow in clay media is an important process for geological disposal of high-level nuclear wastes. Clay/shale formations have been considered as potential host rock for geological disposal of high-level radioactive waste because of their low permeability, low diffusion coefficient, high retention capacity for radionuclide, and capability to self-seal fractures (Tsang et al., 2012). In geologic repositories for radioactive waste disposal, compacted expansive clay soils (bentonites) are also often considered as buffer materials within an engineered barrier system, to be placed in the repository tunnels between the radioactive waste and the host rock. The bentonite is usually compacted at low water content, and then progressively wetted by water from the surrounding host formation. As a result, an unsaturated zone generally develops within the near field of a clay repository. The unsaturated wetting process is accompanied by bentonite swelling which ensures acceptable sealing of open spaces between waste packages and the corresponding host formation. At the same time, heat emanating from the decaying radioactive waste causes thermal gradients and unsaturated flow within the engineered and natural barriers. Accurately modeling unsaturated flow in such clay materials, and how it is related to swelling and heat transfer processes, is critical for assessing the performance of both clay rock and buffer materials for isolating radioactive wastes at a disposal site.

Water flow in porous media is traditionally described by Darcy's law. In 1856, Henry Darcy investigated the flow of water in vertical homogeneous sand filters in connection with the fountains of the city of Dijon in France. From his experiment results, Darcy discovered that water flux is directly proportional to the hydraulic gradient. However, it has been well documented that Darcy's law is not adequate for clay media. For example, Hansbo (1960, 2001) reported that water flux in a low-permeability clay is proportional to a power function of the hydraulic gradient when the gradient is less than a critical value, whereupon the relationship between water flux and gradient becomes linear for large gradient values. He explained this behavior by positing that a certain hydraulic gradient is required to overcome the maximum binding energy of mobile pore water. From their experiment results, Miller and Low (1963) also found the existence of a hydraulic gradient below which water is essentially immobile. After analyzing several data sets for water flow in clay media, Swartzendruber (1961) proposed a modified Darcy's law in which non-linear behavior of water flux vs. gradient is described by an exponential function. Zou (1996) developed a nonlinear flux-gradient relationship depending on the activation energy of pore liquid. He assumed that the activation energy of pore water in clay is not only variable with the distance from the solid particle surface, but also with the flow velocity of pore water. His model, which includes several empirical parameters, is able to fit a number of data sets that show nonlinear flux-gradient relationships at low hydraulic gradients and linear relationships at high gradients.

The studies mentioned above are all for saturated flow conditions. Laboratory test results seem to show that non-Darcian flow behavior becomes even more significant under unsaturated conditions. Cui et al. (2008) reported non-Darcian behavior for a range of observed hydraulic gradients under unsaturated conditions. Liu et al. (2012) developed a constitutive model for unsaturated flow when water can be considered as a power-law (non-Newtonian) fluid. The model is consistent with the data set of Cui et al. (2008).

While considerable progress has been made for investigating non-Darcian flow in clay media, a general relationship between water flux and hydraulic gradient (that covers the full range of non-Darcian flow behavior under both saturated and unsaturated conditions) is still lacking. We will develop such a model in this paper and also demonstrate an empirical relationship between permeability and threshold hydraulic gradient (that will be defined later and is an important measure of non-Darcian behavior). The latter relationship is practically useful because it can reduce the number of parameters whose values need to be determined from experiment data in order to model non-Darcian behavior.

3.2 Relationships between water flux and hydraulic gradient

The key requirement for accurately modeling water flow in clay media is an appropriate relationship between water flux and hydraulic gradient. This section reviews the currently available relationships and develops an improved relationship that can capture a relatively large range of water flow behavior. The well-known flux-gradient relationship is Darcy's law given by

$$q = Ki \qquad (3\text{-}1)$$

where q (m/s) is water flux, K (m/s) is hydraulic conductivity and i (-) is hydraulic gradient. The above equation only includes magnitudes of variables for one-dimensional flow and therefore q, K, and i are all positive. A similar treatment, for convenience, is used for all the other relationships to be discussed in this section.

Darcy's law was initially developed for water flow in saturated porous media. Buckingham (1907) extended Darcy's law to unsaturated conditions, although it is an issue of debate whether he was aware of Darcy's law when developing his relationship. In his extension, Buckingham (1907) used an unsaturated hydraulic conductivity, a function of water saturation, to replace hydraulic conductivity in Darcy's law. An excellent historic review of Edgar Buckingham and his scientific contributions to unsaturated flow in soils was recently published by Nimmo and Landa (2005).

Hansbo (1960, 2001) proposed a relationship between water flux and hydraulic gradient to consider the non-Darcian flow behavior in clay media:

$$\begin{aligned} q &= k^* i^n && \text{for } i \le i_1 \\ q &= k^* n i_1^{n-1}(i - I) && \text{for } i \ge i_1 \end{aligned} \qquad (3\text{-}2)$$

$$\boxed{i_1 = \frac{In}{(n-1)}}$$

The formulation of Hansbo (1960, 2001) includes three parameters k^* (m/s), n (-) and I (-). Note that k* herein is not the hydraulic conductivity and Eq. (3-2) corresponds to a linear function between water flux and hydraulic gradient i. Parameter I is called threshold gradient in this study and refers to the intersection between the i axis and the linear part of the relationship (Figure 1). Hansbo (1960, 2001) demonstrated that Eq. (3-2) can fit related experimental observations and developed, based on (3-2), a theoretical approach to dealing with clay consolidation processes. However, as indicated by Swartzendruber (1961), Eq. (3-2) consists of two separated mathematical expressions and three related parameters cannot be evaluated unless data are available all the way from $i=0$ out to and including an appreciable part of the linear portion of the flux-gradient curve.

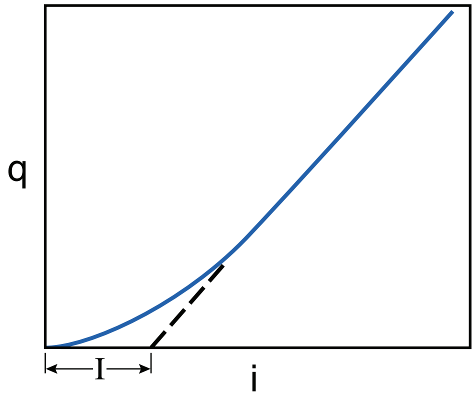

Figure 3-1. Definition of threshold hydraulic gradient

To overcome the difficulties encountered in applying (3-2), Swartzendruber (1961) introduced a new version of the modified Darcy's law based on a relation for dq/di:

$$\frac{dq}{di} = K(1 - e^{-i/I}) \tag{3-3}$$

For a large value of hydraulic gradient i, dq/di approaches a constant K that is hydraulic conductivity. Integrating, and using $q=0$ at $i=0$, leads to

$$q = K[i - I(1 - e^{-i/I})] \tag{3-4}$$

Eq. (3-4) involves two parameters K and I. In contrast to the commonly used Darcy's law, it contains only one additional parameter (I). The equation of Swartzendruber (1961) had been evaluated with a number of data sets collected under saturated flow conditions and satisfactory agreements were generally obtained (Swartzendruber, 1961; Blecker, 1970). However, Figure 3-2 shows a comparison between results calculated from Eq. (3-4) and a data set collected by Cui et al. (2008) under unsaturated flow conditions, indicating a deviation between the theoretical and observed results. Note that under unsaturated conditions, Figure 3-2 shows data for unsaturated permeability that is defined as permeability multiplied by relative permeability for water flow. Thus, Eq. (3-4) cannot capture the full range of non-Darcian flow behavior in clay media under different conditions.

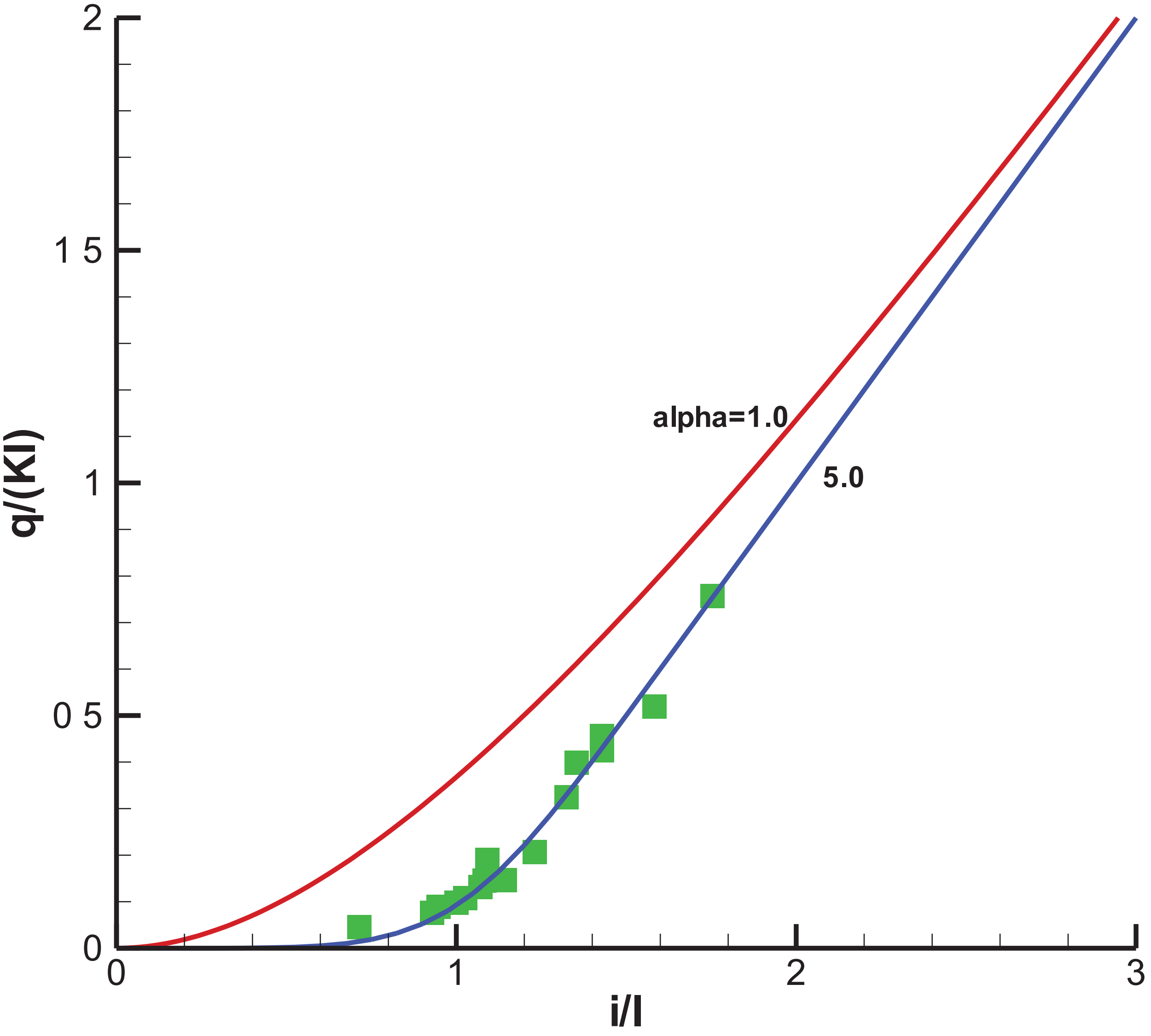

Figure 3-2. Comparisons between proposed Eq. (3-8) with two different values of the parameter α and data of Cui et al. (2008). Note that Eq. (3-8) is reduced to Swartzendruber Equation [Eq. (3-4)] for α=1.

Another commonly used flux-gradient relationship for clay is given as:

$$q = 0 \quad \text{for } i \le I \qquad (3\text{-}5)$$

$$q = K(i - I) \quad \text{for } i \ge I$$

Similar to Eq. (3-4), the above equation involves only two parameters (K and I) and is mathematically simpler than other relationships. It is obvious, however, from data available in the literature, that Eq. (3-5) cannot adequately capture the non-Darcian flow behavior (or non-linear flux-gradient relationship) at low i values (e.g., Swartzendruber, 1961; Blecker, 1970). Therefore, Eq. (3-5) should be applied only when i is large. It is also of interest to note that Eq. (3-5) is a limiting case of Eq. (3-4) for $i/I \rightarrow \infty$.

Assuming that the activation energy of pore water in clay is not only variable with the distance from the solid particle surface, but also with the flow velocity of pore water, Zou (1996) proposed the following flux-gradient relationship:

$$q = \frac{Ki}{1 + b\exp(-ci)} \tag{3-6}$$

where b and c are empirical parameters. One problem with this equation is that it will become exactly the Darcy's law, defined in (3-1), for $i \rightarrow \infty$ without considering the threshold gradient that has been often observed from test results, as shown in Figure 3-2.

From the above discussions, it is clear that a general relationship between water flux and hydraulic gradient (that covers full range of non-Darcian flow behavior under both saturated and unsaturated conditions) is still lacking. As an effort to overcome this problem, we propose to generalize the Swartzendruber's (1961) relationship by using

$$\frac{dq}{di} = K(1 - e^{-\left(\frac{i}{I^*}\right)^{\alpha}}) \tag{3-7}$$

where α is a positive constant, and I^* is a parameter related to α and I. For $\alpha = 1$, (3-7) is reduced to Eq. (3-3). For $\alpha \rightarrow \infty$, $\frac{dq}{di} \rightarrow 0$ when $\frac{i}{I^*} < 1$, and $\frac{dq}{di} \rightarrow K$ when $\frac{i}{I^*} > 1$. In this case, Eq. (3-7) essentially represents the flux-gradient behavior given in Eq. (5). Thus, with one more parameter (α), (3-7) can capture a relatively large range of non-Darcian flow behavior.

Integrating (3-7) with the condition of $q=0$ at $i=0$ yields

$$q = K[i - \frac{I}{\gamma(\frac{1}{\alpha})}\gamma(\frac{1}{\alpha}, \left(\frac{i}{I^*}\right)^{\alpha})] \tag{3-8}$$

where

$$I = \frac{I^*}{\alpha}\gamma\left(\frac{1}{\alpha}\right) \tag{3-9a}$$

and γ refers to Gamma functions

$$\gamma(a,x) = \int_0^x t^{a-1}e^{-t}dt \tag{3-9b}$$

$$\gamma(a) = \int_0^\infty t^{a-1}e^{-t}dt \tag{3-9c}$$

Figure 2 shows a good agreement between Eq. (3-8) with $\alpha = 5$ and the data from Cui et al. (2008). Note that Cui et al. (2008) reported flux-gradient data for three capillary pressure values. Each capillary pressure has its own I value. Different I values are used in Figure 2 for different capillary pressure when calculating i/I and dimensionless flux defined as $q/(KI)$.

3.3 Correlation between permeability and threshold gradient

Previous studies suggest that non-Darcian flow is a result of strong solid-water interaction in clay materials. Since pore size in clay media is on the order of nanometers, studies of water properties and flow processes in nanotubes are highly relevant to water flow in clay (Wang et al., 2011a). The mechanism of non-Darcian flow behavior was attributed to water-clay interaction by Low (1961). This is further confirmed by a number of studies on nanoscale fluid transport based on molecular dynamics (MD) simulations (e.g., Chen et al., 2008; Ma et al., 2010; Farrow et al., 2011). These studies generally show that water properties and flow processes at that scale could be significantly different from those in less fine-grained materials. For example, the density of water near the solid surface of grain material is generally much higher than its bulk value. It has been widely accepted for porous media that owing to viscous forces, the water velocity can be assumed zero on the solid surface. This non-slippage boundary condition, however, does not apply to nanoscale flow because of the sub-continuum behavior of water molecules. Also, the resistance to water flow at the nanoscale is dominantly from friction between water and solid surfaces, and less so from internal friction between water layers, because of the small pore sizes (Chen et al., 2008). Several MD simulation results show that the flow rate of water through a nanotube is a nonlinear function of shearing stress (equivalent to hydraulic gradient for steady-state flow) (e.g., Chen et al., 2008; Ma et al., 2010; Farrow et al., 2011), which is consistent with non-Darcian behavior observed from laboratory measurements.

For a clay material, the degree of solid-water interaction and non-Darcian flow behavior can be characterized by permeability (K) (or pore size) and threshold gradient (I), respectively. Thus, it seems logical to expect a correlation between K and I. We will demonstrate such a relationship using a number of typical clay data sets of permeability vs. gradient (Figure 3-3). This correlation, if it can be demonstrated, would be very important because the number of parameters in Eq. (3-8) (whose values are required for practical applications) would be reduced. For better transparency, the data sets and procedures to determine parameter I and permeability are briefly given in the rest of this section, while we refer the readers to the cited references for the details of the data sets.

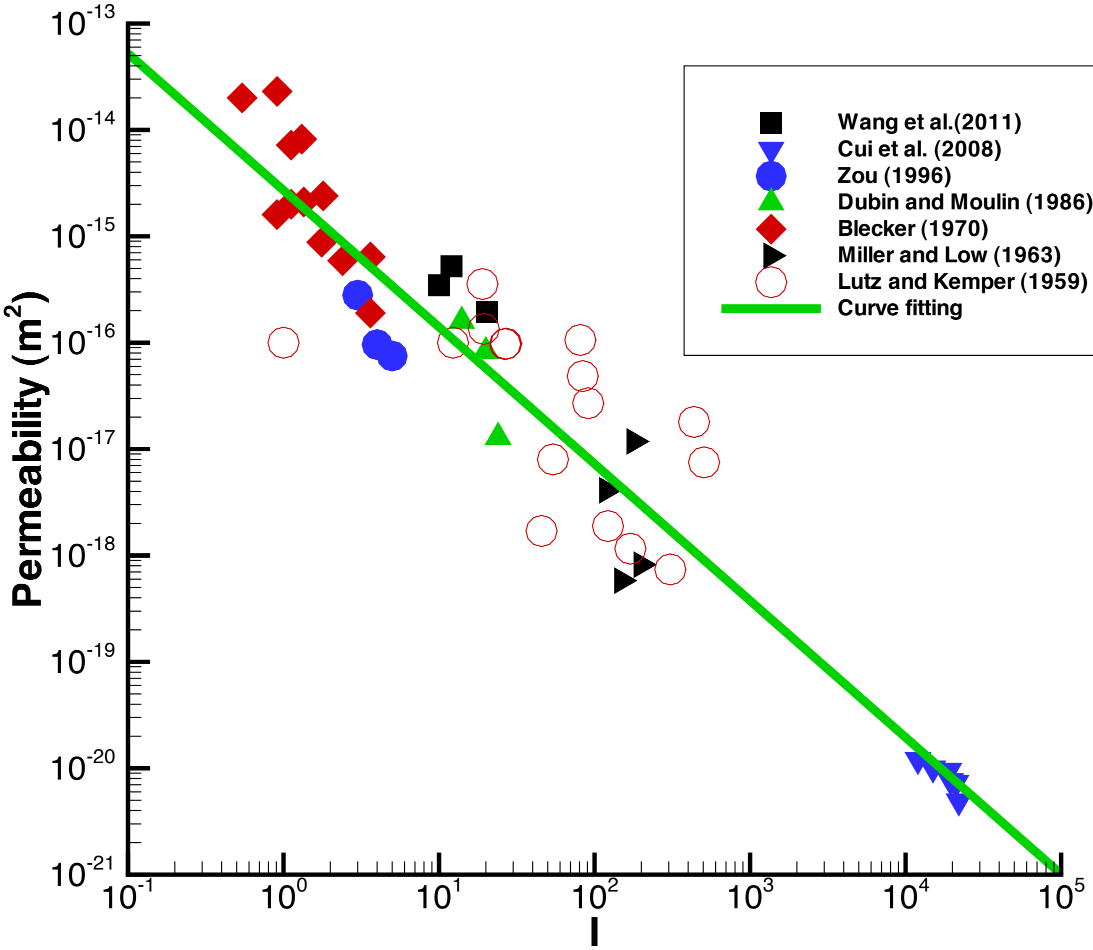

Figure 3-3. Correlation between permeability and threshold hydraulic gradient.

Miller and Low (1963) presented results of laboratory experiments for Wyoming bentonite. The soil samples have a length of 2.5 cm and diameter of 1 cm. Rates for water flow through soil samples were measured as a function of hydraulic gradient. We estimated permeability values using the slope of the linear part of the flow-rate versus gradient curve. When the data points corresponding to the linear part are limited, we use a straight line through the two data points with the highest gradient values to approximate the linear part. Note that Miller and Low (1963) defined their threshold gradient as the gradient below which water does not flow, while here we use the term threshold gradient *I*, as previously indicated, to describe the intersection between the gradient axis and the linear part of the flux-gradient relationship (Figure 1). Figure 4 shows a match of Eq. (3-8) with data from one of the experiments conducted by Miller and Low (1963). The fitted α value is 0.9, indicating that the relationship of Swartzendruber (1961), corresponding to α = 1, should give a similar match.

Blecker (1970) reported test results regarding flux-gradient relationships for clay soils from Brolliar and Springerville soil series of northern Arizona, USA. His experimental setup is similar to the one used by Miller and Low (1963). The soil samples were prepared with different densities for a given soil type. His data show a good agreement with Eq. (3-4). He also reported values for all the fitting parameters including permeability and *I*. However, his reported values for hydraulic head difference across a soil sample are based on heights of mercury column. To be consistent with other data sets in Figure 3-3, we converted his reported values by representing the head difference with height of water column.

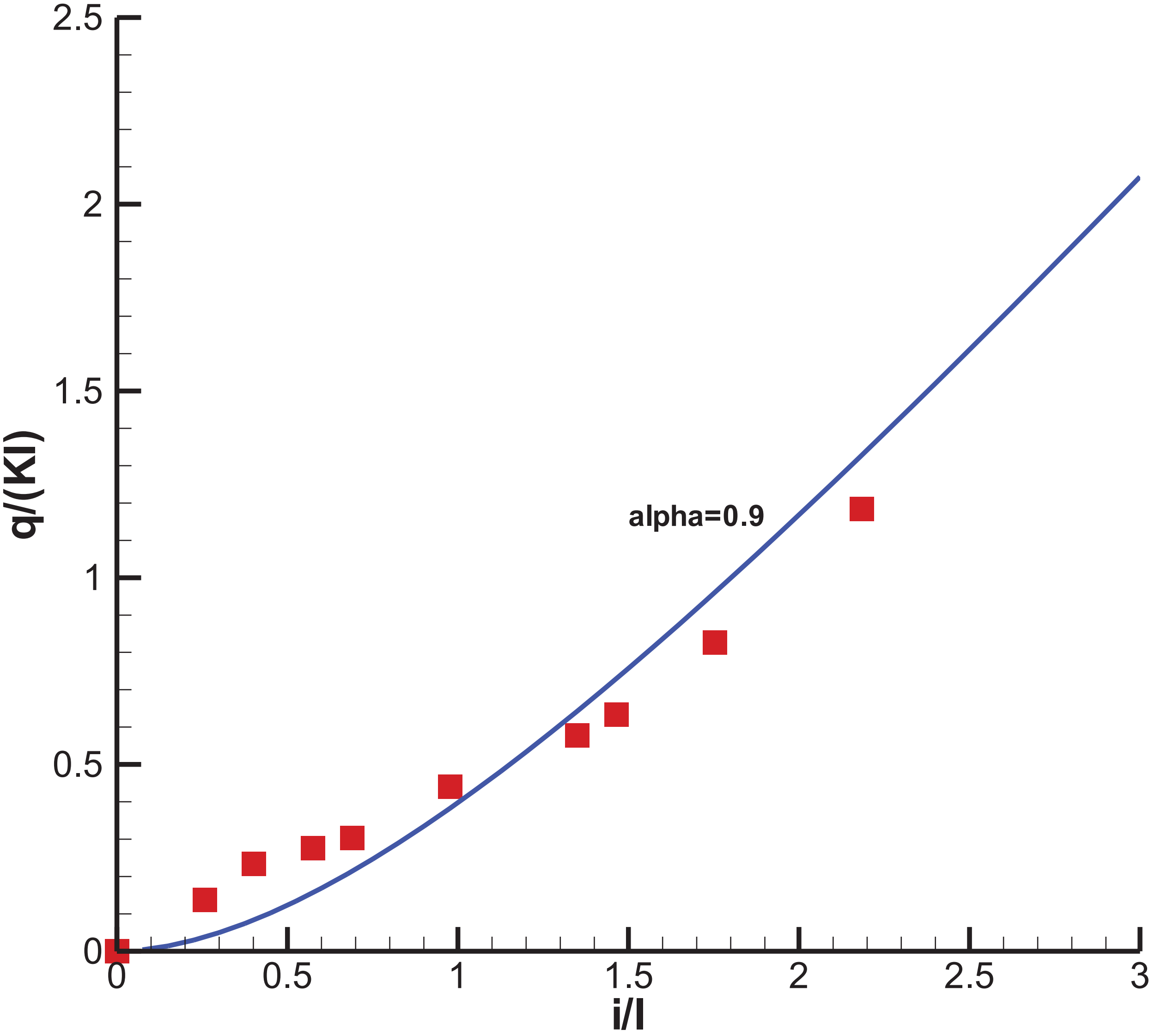

Figure 3-4. Match of Eq. (8) with test data for a Na-clay paste (Miller and Low, 1963).

Consolidation of clays is important for some civil-engineering applications. Investigation of consolidation behavior requires data of clay permeability under different mechanical and hydraulic conditions (Hansbo, 2001). For this purpose, Dubin and Moulin (1986) reported measured flux-gradient curves for Saint Herblain clay (their Figure 7). The corresponding hydraulic conductivity values were converted to permeability values in Figure 3-3. To evaluate his relationship for water flux and hydraulic gradient, Zou (1996) also presented a data set for several soil types. Figure 3-3 only shows his data points for clay soil because no significant non-Darcian behavior is observed from other soils in his paper.

Wang et al. (2011a) presented test data from core samples collected from low-permeability Daqing oilfield, China. During their tests, core samples were first saturated with salt water (composition is not available), and then a pressure gradient across them was imposed. After steady-state flow conditions were achieved, the water flux value was recorded. In this way, they were able to generate flow rate data as a function of hydraulic gradient. The non-Darcian flow behavior is represented by the ratio of $(\frac{q}{i})/K$ (their Figure 2) in terms of variables defined in this paper. The permeability values reported in Wang et al. (2011a), with appropriate unit conversion, are used in Figure 3-3. Based on (4), the ratio $(\frac{q}{i})/K$ can be expressed as

$$\frac{q/i}{K} = 1 - \frac{1 - e^{-\frac{i}{I}}}{i/I} \qquad (3\text{-}10)$$

The above equation is used to fit the data sets of Wang et al. (2011a). A comparison between calculated curve and the data is given in Figure 5. The fitted *I* values are 20.4, 12.0 and 10.0 for rock samples with permeability values of 0.195 mD, 0.347 mD and 0.524 mD, respectively. The comparison between data and (3-10) is reasonable, suggesting that Eq. (3-4) is valid for describing flux-gradient relationships for these rock samples.

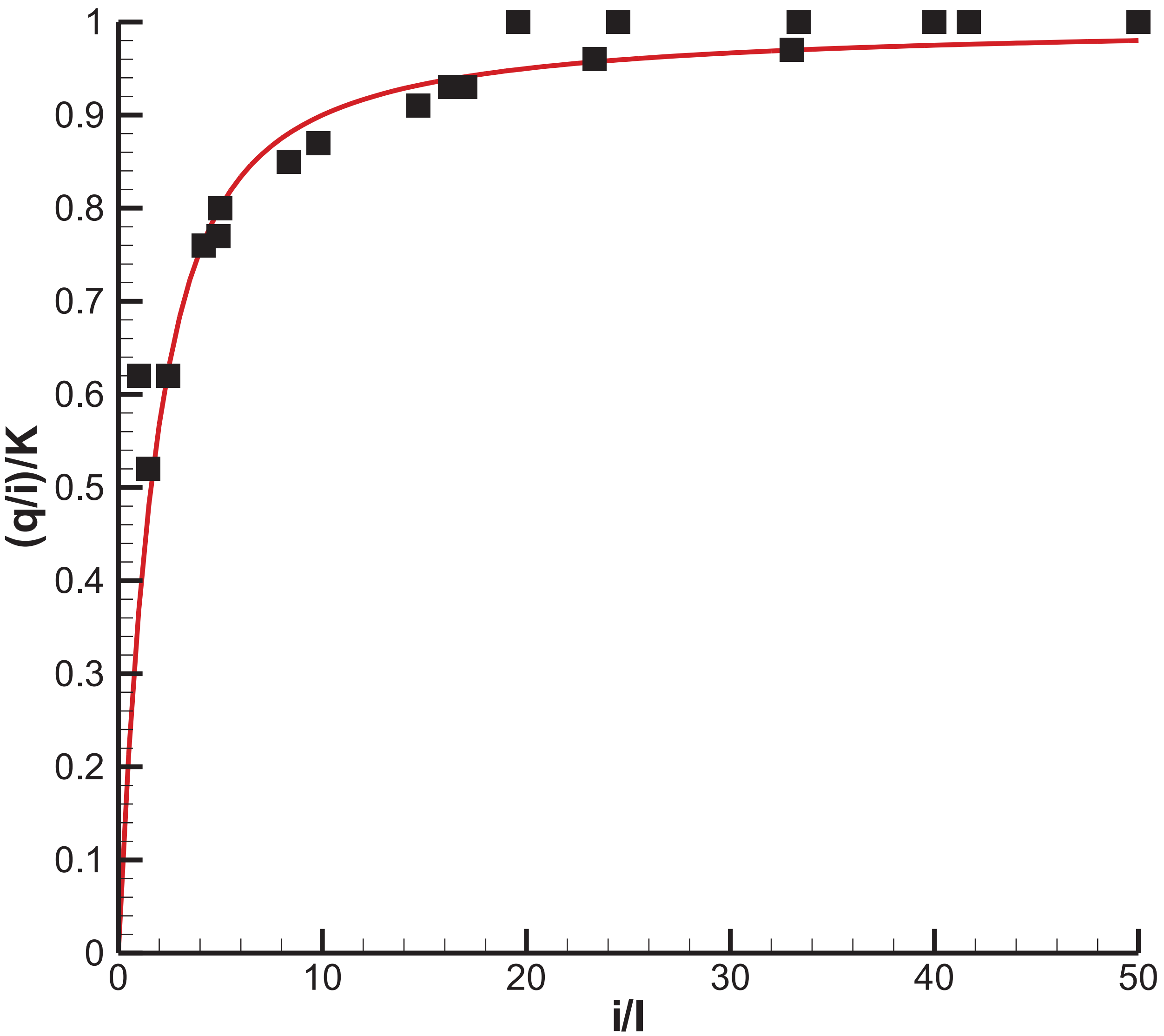

Figure 3-5. Match of Eq. (10) with test data of Wang et al. (2011a).

Lutz and Kemper (1959) were among the first to report the impact of clay-water interaction on clay hydraulic properties. The types of clay soils used in their tests include Utah bentonite, hallosite, Bladen clay, and Wyoming bentonite. The tests were conducted under saturated conditions using solutions with different electrolyte concentrations. For the given soil and hydraulic gradient, a low concentration generally corresponds to a low water flow rate, as a result of swelling. During their tests, water flow rate was monitored as a function of the gradient. The threshold values for all these tests were calculated by Swartzendruber (1961) and used in Figure 3-3. Swartzendruber (1961) also demonstrated that the data are consistent with Eq. (3-4). A cross-sectional area of soil samples is needed to determine permeability values from the flow rate versus gradient data at large gradients corresponding to Darcy behavior. However, Lutz and Kemper (1959) did not report the value of the area, only the thickness of soil samples. Thus, we determine the area value from the ratio of sample diameter to its thickness value measured from the test-setup figure in Lutz and Kemper (1959). Since this approximation may involve significant uncertainties, the data of Lutz and Kemper (1959 are not used for estimating the relationship between parameter *I* and permeability in Figure 3-3; they have been plotted in Figure 3-3 to provide corroborative information. Nevertheless, the data seems to be consistent with the general trend in the figure. Also note that impact of soil swelling for this and other data sets to be discussed, to some extent, has been included in permeability values because permeability is a strong function of swelling (or shrinkage).

All the data sets discussed above are for saturated conditions. Cui et al. (2008) reported measurements of unsaturated hydraulic conductivity for a compacted sand-bentonite mixture. To the best of our knowledge, this work provided the first reliable data set of water flux as a function of hydraulic gradient under unsaturated conditions. The tests of Cui et al. (2008) were conducted under two experimental boundary conditions: constant volume and free swelling. In this study, we focus on the data for constant-volume conditions, based on the reasoning that under constant-volume conditions and for a given capillary pressure, hydraulic processes and pore structures are approximately the same at different locations within the soil sample (Cui et al., 2008). Cui et al. (2008) used the instantaneous profile method to determine the unsaturated hydraulic conductivity for infiltration tests of a vertical sand-bentonite column. The sand-bentonite mixture was directly compacted in a metallic cylinder (50 mm in inner diameter, 250 mm high). The bottom of the test cell was connected to a water source, and the upper end to an air source under atmospheric pressure. Under transient water-flow conditions, vertical distributions of capillary pressure were directly measured as a function of time at several locations along the column. The relationship between water content and capillary pressure was independently measured under constant volume conditions. This relationship enables them to estimate vertical distributions of water content from the capillary-pressure measurements. Based on these vertical distributions at different times, and assuming mass balance at each location within the soil column, they estimated the water flux at that location as a function of capillary pressure and hydraulic gradient (their Figure 12). The details of this instantaneous method can be found in Cui et al. (2008). For this study, linear part of the flux-gradient relationship for a given capillary pressure is approximated by a straight line through the two points with the largest hydraulic gradients. Consequently, the unsaturated permeability (relative permeability for water multiplied by absolute permeability) and the threshold gradient I can be obtained for each capillary pressure. Figure 3-3 shows the match between Eq. (3-8) and the data set.

As shown in Figure 3-3, the data sets can be reasonably fitted by a relationship between I and permeability k (m^2)

$$I = Ak^B \qquad (3\text{-}11)$$

with $A = 4.0 \times 10^{12}$ and $B = -0.78$. This is very encouraging considering that the data sets were collected for different kinds of clay media and low-permeability materials and by different researchers. This may imply the existence of a universal relationship between I and permeability, although some degree of fluctuation exists in Figure 3-3.

Equation (3-11) (or Figure 3-3) can be used to evaluate the relative importance of non-Darcian behavior for a given media if its permeability is known. For example, non-Darcian behavior can be safely ignored for permeability values larger than 10^{-13} m^2 based on Figure 3-3. Also, when data are not available for estimating site-specific values for A and B, Eq. (3-11) can be directly used for estimating parameter I based on more easily obtained permeability values. Eq. (3-11) is also useful in providing a criterion for permeability to be accurately measured. For example, if the hydraulic gradient head used in tests is less than the value calculated from Eq. (3-11), the measured permeability will depend on the gradient and does not correspond to the correct value.

It is especially of interest that the data for unsaturated flow follow the same relationship as for saturated flow if permeability is replaced by unsaturated permeability (relative permeability multiplied by permeability) (Figure 3-3). This is because unsaturated permeability is related to the sizes of pores occupied by water under unsaturated conditions. In practical applications, it is very difficult, if not impossible, to determine the parameter I for different capillary pressures. Figure 3-3 seems to indicate that the same A and B values can be used for different capillary pressures, although this needs to be further confirmed when more data are available. If this is the case, A and B values can be either estimated from data at one capillary pressure or using values from Figure 3-3 when site-specific data are not available. Then *I* values for different capillary pressures (or saturations) can be estimated from Eq. (3-11) using unsaturated permeability. The relationships between unsaturated permeability and capillary pressures are well established for unsaturated media (van Genuchten, 1980; Brooks and Corey, 1964).

3.4 Discussion

We developed a new relationship for one-dimensional water flow and hydraulic gradient given in Eq. (3-8). It can be considered a generalization of two previous formulations (Eqs. (3-4) and (3-5)) and is more consistent with laboratory experiments. In many studies, we need to investigate multidimensional water-flow processes. For that purpose, we extend Eq. (3-8) to three-dimensional, homogeneous and isotropic clay media:

$$\mathbf{q} = -K\left[i - \frac{I}{\gamma(\frac{1}{\alpha})}\gamma\left(\frac{1}{\alpha},\left(\frac{i}{I^*}\right)^{\alpha}\right)\right]\mathbf{n_i} \qquad (3\text{-}12)$$

where q (m/s) and $\mathbf{n_i}$ (-) are water flux vector and unit vector for hydraulic gradient, respectively. The relationship between I and I^* is given by (3-9). When the threshold gradient I approaches zero, Eq. (3-12) is reduced to the commonly used form of Darcy's law. It should be emphasized that Eq. (3-12) is an empirical relationship and developed based on one dimensional test results. It is logical to directly extend Eq. (3-8) to Eq. (3-12) for homogeneous and isotropic cases because both equations are consistent with the one-dimensional-test condition that flux and negative hydraulic gradient are along the same direction. That condition is violated for three-dimensional anisotropic porous media. In this case, it is not clear whether Eq. (3-12) is adequate.

Eq. (3-12) is applicable to both saturated and unsaturated flow processes. As demonstrated in Figure 3-2, Eq. (3-12) can also be used to satisfactorily describe unsaturated flow, although the related flux-gradient data are very limited. For unsaturated flow, both hydraulic conductivity and threshold gradient *I* are dependent on capillary pressure or water saturation. In this regard, the developed relationship between permeability and *I* (Eq. (3-11)) is especially useful. As previously indicated, it is practically difficult, if not impossible, to experimentally obtain flux-gradient data under constant capillary pressures (or saturations) to determine the threshold gradient *I* for a large range of capillary-pressure values. However, through the relationship given in Eq. (3-11), we can easily obtain *I* from unsaturated permeability whose dependence on saturation and capillary pressure has been well established.

It is not clear how parameter α is related to other clay parameters, while a single α value cannot adequately capture all the non-Darcian flow behavior of interest, as demonstrated in Figures 3-2 and 3-4. One speculation is that parameter α may be related to pore-size distribution, because the observed flux-gradient relation is a combination of water flow processes across pores with different sizes that correspond to different degrees of water-solid interaction. Nevertheless, this needs to be further confirmed in future studies.

Finally, parameters in Eq. (3-12) depend on the electrolyte concentration of solution that flows through clay media and on its temperature. For example, Swartzendruber (1961) analyzed the data of Lutz and Kemper (1959) that were collected for solutions with different electrolyte concentrations and found that the threshold gradient decreases with the concentration. As previously indicated, the impact of the concentration is partially considered herein through the correlation between permeability and *I* (Eq. (3-11)). For example, with increasing solution concentration, permeability will increase because of shrinkage and thus parameter *I* will decrease based on Eq. (3-11), which is consistent with the analysis results of Swartzendruber (1961). Studies of temperature impact on non-Darcian behavior are rare in the literature. To the best of our knowledge, the only study that is related to temperature impact is Miller and Low

(1963). They experimentally found that the critical hydraulic gradient (below which water is immobile) decreases with increasing temperature. They argue that this is because increased temperature may weaken the bounding between water molecules and clay surface. More experimental and theoretical studies are needed to fully establish temperature dependence of related parameters in Eq. (3-12).

3.5 Summary

Water flow in clay media is an important process for a number of practical applications. Experimental results indicate that the traditional form of Darcy's law is not adequate for describing water flow processes in clay media because the observed relationship between water flux and hydraulic gradient can be highly non-linear. In this paper, to capture this non-Darcian flow behavior, we developed a new relationship between water flux and hydraulic gradient by generalizing the currently existing relationships. The new relationship is shown to be consistent with experimental observations for both saturated and unsaturated conditions. We also developed an empirical relationship between permeability and the threshold hydraulic gradient, an important measure of non-Darcian behavior. The latter relationship is practically useful because it can reduce the number of parameters whose values need to be determined from experiment data in order to model non-Darcian behavior. However, how to incorporate the impacts of temperature and electrolyte concentrations into the proposed relationships requires further research.

4. REFERENCES

Amemiya T., 1985. Advanced Econometrics. Harvard University Press.

Arbogast T., Cowsar L. C., Wheeler M. F., Yotov I., 2000. Mixed finite element methods on non-matching multiblock grids, SIAM Journal Numerical Analysis 37(4), 1295-1315.

Barenblatt, G.I., Zheltov Y.P., Kochina I.N., 1960. Basic concepts in the theory of seepage of homogeneous liquids in fissured rocks. Journal of Applied Mathematics of Mechanics (English Translation) 24, 1286–1303.

Botros F. E., Hassan A. E., Reeves D. M., and Pohll G., 2008. On mapping fracture networks onto continuum, Water Resources Research 44, W08435, doi:10.1029/2007WR006092.

Blecker, R.F., 1970. Saturated flow of water through clay loam subsoil material of the Brolliat and Springerville soil series. Master's Thesis, The University of Arizona.

Brooks, R. H., and Corey, A. T., 1964. Hydraulic properties for porous media. Hydro. Rep. No. 3, Colorado State University, Fort Collins.

Buckingham, E. 1907. Studies on the movement of soil moisture. Bulletin 38. USDA Bureau of Soils, Washington, DC.

Chen, X., Cao, G.X., Han, A.J., Punyamurtula, V.K., Liu, L., Culligan, P.J., Kim, T., and Qiao.Y., 2008. Nanoscale fluid transport: size and rate effects. Nano Letters, 8(9), 2988-2992.

Cordes C. and Kinzelbach W., 1992. Continuous groundwater velocity field and path lines in linear, bilinear, and trilinear finite elements, Water Resources Research 28(11), 2903-2911.

Cui, Y.J., Tang, A. M., Loiseau, C., and Delage P., 2008. Determining the unsaturated hydraulic conductivity of a compacted sand-bentonite mixture under constant-volume and free-swell conditions. Physics and Chemistry of the Earth 33, S462-S471.

Cvetkovic V., Painter S., Outters N., and Selroos J.-O., 2004. Stochastic simulation of radionuclide migration in discretely fractured rock near Aspo hard rock laboratory, Water Resources Research 40, W02404, doi:10.1029/2003WR002655.

de Berg M., Cheong O., van Kreveld M., Overmars M., 2008. Computational Geometry: Algorithms and Applications. Springer-Verlag. ISBN 978-3-540-77973-5.

Delaunay B., 1934. Sur la sphère vide, Izvestia Akademii Nauk SSSR, Otdelenie Matematicheskikh i Estestvennykh Nauk, 7:793–800.

Dubin, B., and Moulin, G., 1986. Influences of critical gradient on the consolidation of clay. In Consolidation of soils, testing and evaluation (eds Young and Townsend), ASTM STP 892, pp. 354-377. West Conshohocken, PA.

Duguid J.O. and Lee P. C. Y., 1977. Flow in fractured porous rock, Water Resources Research 13, 558–566.

Erhel J., de Dreuzy J.R., Poirriez B., 2009. Flow simulation in three-dimensional discrete fracture networks, SIAM Journal on Scientific Computing 31(4), 2688-2705.

Ewing R., Lazarov R., Lin T., and Lin Y., 2000. The mortar finite volume element methods and domain decomposition. East-West Journal of Numerical Mathematics 8, 93–110.

Farrow, M.R., Chremos, A., Camp, P.J., Harris, S.G., and Watts, R.F., 2011. Molecular simulations of kinetic-friction modification in nanoscale fluid layers. Tribol Lett. 42, 325-337.

Hansbo, S. 1960. Consolidation of clay, with special reference to influence of vertical sand drains. Swed. Geotech. Inst. Proc. 18, Stockholm.

Hansbo, S., 2001. Consolidation equation valid for both Darcian and non-Darcian flow. Geotechnique 51(1), 51-54.

Jackson, C., Hoch, A., Todman, S., 2000. Self-consistency of a heterogeneous continuum porous medium representation of a fractured medium, Water Resour. Res. 36 (1), 189-202.

Joyce S., Simpson T., Hartley L., Applegate D., Hoek J., Jackson P., Swan D., Marsic N., Follin S., 2010. Groundwater flow modelling of periods with temperate climate conditions – Forsmark. SKB R-09-20, Svensk Kärnbränslehantering AB.

Karimi-Fard M., Gong B., Durlofsky L. J., 2006. Generation of coarse-scale continuum flow models from detailed fracture characterizations. Water Resources Research 42 (10) W10423.

Los Alamos Grid Toolbox, LaGriT (2011) Los Alamos National Laboratory, <http://lagrit.lanl.gov>.

Liu, H.H., Li, L.C., and Birkholzer, J., 2012. Unsaturated properties for non-Darcian water flow in clay. Journal of Hydrology, 430-431, 173-178.

Low, P.F., 1961. Physical chemistry of clay-water interaction, Advances in Agronomy, 13, 269-327.

Lutz, J.F., and Kemper, W.D., 1959. Intrinsic permeability of clay as effected by clay-water interaction. Soil Sci. 88, 83-90.

Ma, M., Shen, L., Sheridan, J., Liu, Z., Chen C., and Zheng, Q., 2010. Friction law for water flowing in carbon nanotubes. 2010 International Conference on Nanoscience and Nanotechnology. Feb. 20-22, Sydney, Australia.

Maryska, J. Severyn, O. Vohralk, M., 2005. Numerical simulation of fracture flow with a mixed-hybrid fem stochastic discrete fracture network model, Computat. Geosci. 8 (3) 2170-234.

Miller, R.J., and Low P.F., 1963. Threshold gradient for water flow in clay systems. Soil. Sci. Soc. Am. Proc. 27(6), 605-609.

Mosé R., Siegel P., Ackerer P., and Chavent G. (1994) Application of the mixed hybrid finite element approximation in a groundwater flow model: Luxury or necessity?, Water Resources Research 30(11), 3001–3012, doi:10.1029/94WR01786.

Murphy M., Mount D. M., Gable C. W., 2001. A Point-Placement Strategy for Conforming Delaunay Tetrahedralization, International Journal of Computational Geometry and Applications 11, 669-682.

Mustapha H., Dimitrakopoulos R., 2009. Discretizing two-dimensional complex fractured fields for incompressible two-phase flow, International Journal for Numerical Methods in Fluids 65 (7), 764-780.

Mustapha H., 2010. G23FM: a tool for meshing complex geological media, Computational Geosciences 15 (3) 385-397, DOI: 10.1007/s10596-010-9210-6.

Mustapha H., Dimitrakopoulos R., Graf T., Firoozabadi A., 2010. Discretizing Complex Fractured Media for Flow and Transport Simulations, American Institute of Physics Conference Proceedings 1281, 1566-1570.

National Research Council (1996) Rock Fractures and Fluid Flow: Contemporary Understanding and Applications, National Academies Press, Washington.

Nimmo, J. R., and Landa, E.R., 2005. The soil physics contributions of Edgar Buckingham. Soil. Sci. Am. J. 69:328-342.

Neuman, S. P., 1987. Stochastic continuum representation of fractured rock permeability as an alternative to the REV and discrete fracture concepts. In Farmer I.W., Daemen J. J. K., Desai C.S., Glass C.E. Neuman S. P. (eds) Rock Mechanics, Proceedings of the 28th US Symposium, Tucson, Arizona. AA Balkema, Rotterdam.

Neuman, S. P., 2005. Trends, prospects and challenges in quantifying flow and transport through fractured rocks, Hydrogeology Journal 13, 124–147.

Okabe A., Boots B., Sugihara K., Chiu S. N., 1992. Spatial Tessellations: Concepts and Applications of Voronoi Diagrams, John Wiley & Sons.

Ruppert, J., 1995. A delaunay refinement algorithm for quality 2-dimensional mesh generation, J. Algorithms 18 (3) 548-585.

Painter S. and Cvetkovic V., 2005. Upscaling discrete fracture network simulations: An alternative to continuum transport models, Water Resources Research 41, W02002, doi:10.1029/2004WR003682.

Painter S., Cvetkovic V., Mancillas J., and Pensado O., 2008. Time domain particle tracking methods for simulating transport with retention and first-order transformation, Water Resources Research 44, W01406, doi:10.1029/2007WR005944.

Painter S., Gable C., and Kelkar S., 2011. Pathline tracing on fully unstructured control volume grids. Computational Geosciences 16(4) 1125–1134.

Pichot G., Erhel, J., de Dreuzy, J. R., 2010. A mixed hybrid Mortar method for solving flow in discrete fracture networks. Applicable Analysis: An International Journal 89 (10), 1629–1643.

Pruess K. and Narasimhan, T.N., 1985. A practical method to modeling fluid and heat flow in fractured porous media. Society Petroleum Engineers Journal 25(1), 14–26.

Pruess K., Oldenburg C., and Moridis G., 1999. TOUGH2 Users Guide, Version 2.0, LBNL-43134, Lawrence Berkeley National Laboratory, Berkeley CA.

Shewchuk J. R., 1996. Triangle: Engineering a 2D Quality Mesh Generator and Delaunay Triangulator, First Workshop on Applied Computational Geometry (Philadelphia, PA), 124-133, ACM, May 1996, <www.cs.cmu.edu/~quake/triangle.html>.

Si H., 2004. TetGen: A quality tetrahedral mesh generator and three-dimensional Delaunay triangulator, software <http://tetgen.berlios.de/files/tetgen-manual.pdf>.

Svensk Kärnbränslehantering AB, 2011. Long-term safety for the final repository for spent nuclear fuel at Forsmark, SKB TR-11-01, Svensk Kärnbränslehantering AB

Svensson U., 2001. A continuum representation of fracture networks: Part I. Method and basic test cases, Journal of Hydrology 250, 170–186.

Swartzendruber, D. 1961. Modification of Darcy's law for the flow of water in soils. Soil Science 93: 22-29. Soil. Sci. Soc. Am. J. 69, 328-342.

Tsang, C.F., Barnichon, J.D., Birkholzer, J., Li X.L, Liu, H.H., Sillen, X., 2012. Coupled thermo-hydro-mechanical processes in the near field of a high-level radioactive waste repository in clay formations. Int. J. Rock Mech. Min. Sci. 49: 31-44. DOI 10.1016/j.ijrmms.2011.09.015.

Van Genuchten, M., 1980. A closed-form equation for predicting the hydraulic conductivity of unsaturated soil. Soil. Sci. Soc. Am. J. 44(5), 892-898.

Wang, Y.F., 2011. Research and Development Plan for Natural System Evaluation and Tool Development. U.S. Department of Energy.

Wang, X.X., Yang, Z. M., Sun, Y.P., and Liu, X.X., 2011a. Experimental and theoretical investigation of nonlinear flow in low permeability reservoir. Procedia Environmental Sciences, 11, 1392-1399.

Wang, Y.F., Gao, H.Z., and Xu, H.F., 2011b. Nanogeochemistry: nanostructures and their reactivity in natural systems. Frontiers in Geochemistry: contributions of geochemistry to the study of the earth (eds. Russell S. Harmon and Andrew Parker), Blackwell Publishing Ltd.

Warren J.E. and Root P.J., 1963. The behavior of naturally fractured reservoirs. Society of Petroleum Engineers Journal 3, 245–255.

Zou, Y., 1996. A non-linear permeability relation depending on the activation energy of pore liquid. Geotechnique 46(4), 769-774.

Zyvoloski G. A., 2007. FEHM: A control volume finite element code for simulating subsurface multi-phase multi-fluid heat and mass transfer. Los Alamos Unclassified Report LA-UR-07-3359.

Zyvoloski G. A, Robinson B. A, Viswanathan H. S., 2008. Generalized dual porosity: A numerical method for representing spatially variable sub-grid scale processes, Advances in Water Resources 31 (3) 535–544, DOI: 10.1016/j.advwatres.2007.11.006